nature cancer

ARTICLES

https://doi.org/10.1038/s43018-020-0082-y

Cancer-associated fibroblast compositions change with breast cancer progression linking the ratio of S100A4$^+$ and PDPN$^+$ CAFs to clinical outcome

Gil Friedman[1], Oshrat Levi-Galibov[1], Eyal David[2], Chamutal Bornstein[2], Amir Giladi[2], Maya Dadiani[3], Avi Mayo[4], Coral Halperin[1], Meirav Pevsner-Fischer[1], Hagar Lavon[1], Shimrit Mayer[1], Reinat Nevo[1], Yaniv Stein[1], Nora Balint-Lahat[5], Iris Barshack[5,6], H. Raza Ali[7], Carlos Caldas[7,8,9], Einav Nili-Gal-Yam[10], Uri Alon[4], Ido Amit[2] ✉ and Ruth Scherz-Shouval[1] ✉

Tumors are supported by cancer-associated fibroblasts (CAFs). CAFs are heterogeneous and carry out distinct cancer-associated functions. Understanding the full repertoire of CAFs and their dynamic changes as tumors evolve could improve the precision of cancer treatment. Here we comprehensively analyze CAFs using index and transcriptional single-cell sorting at several time points along breast tumor progression in mice, uncovering distinct subpopulations. Notably, the transcriptional programs of these subpopulations change over time and in metastases, transitioning from an immunoregulatory program to wound-healing and antigen-presentation programs, indicating that CAFs and their functions are dynamic. Two main CAF subpopulations are also found in human breast tumors, where their ratio is associated with disease outcome across subtypes and is particularly correlated with *BRCA* mutations in triple-negative breast cancer. These findings indicate that the repertoire of CAF changes over time in breast cancer progression, with direct clinical implications.

Tumors initiate as a clonal disease and grow as ecosystems, in which distinct subpopulations of cells engage in complex interactions. Genetic and epigenetic heterogeneity among cancer cells flows from the intrinsic biology of multistep carcinogenesis[1–3]. Tumors, however, contain more than just cancer cells and the complexity of tumor heterogeneity is amplified by contributions from the tumor microenvironment (TME)[4].

Key players in the TME are CAFs. CAFs promote cancer phenotypes including proliferation, invasion, extracellular matrix (ECM) remodeling and inflammation[4–7], as well as chemoresistance[8] and immunosuppression[9]. Different cell-surface markers identify unique subpopulations of CAFs and different origins have been suggested for CAFs, including tissue-resident fibroblasts, myofibroblasts, bone-marrow (BM)-derived mesenchymal stem cells (MSCs) and adipocytes[10–14].

Currently, it is unclear to what extent CAF subpopulations and their functions change over time with tumor progression and metastasis. Here we address this question using an unbiased approach that does not require a priori defined markers[15] to characterize thousands of CAFs at several time points over breast tumor growth and metastasis in mice. We identify eight CAF subtypes in two main CAF populations, which we term pCAF and sCAF, based on selective expression of the markers *Pdpn* or *S100a4* (also called fibroblast-specific protein 1; FSP1). These CAF subtypes appear progressively over time, transitioning from an early immunoregulatory transcriptional program, to a late combination of antigen-presentation and wound-healing programs. Using the PDPN and S100A4 protein markers, as well as markers for subpopulations of sCAFs and pCAFs, we show that human breast tumors have similar CAF compositions and that the ratio between PDPN$^+$ and S100A4$^+$ CAFs is associated with *BRCA* mutations in triple-negative breast cancer (TNBC). Moreover, in two independent cohorts of patients with breast cancer, the ratio between PDPN$^+$ and S100A4$^+$ CAFs strongly correlates with clinical outcome. This study shows that CAF functions change with tumor progression, providing clinically relevant markers. Our findings raise the concept of a dynamic TME, in which genomically stable cells change their transcriptional program to keep track of the evolving tumor ecosystem.

Results

Comprehensive mapping of breast CAFs reveals subpopulations with distinct transcriptional programs. To discover CAF subtypes associated with breast cancer progression we first set out to characterize the stromal cell types/states that comprise breast tumors in a mouse model of triple-negative 4T1 cancer cells orthotopically injected into the mammary fat pad of immunocompetent BALB/c mice. This cell line has been extensively used as a robust model for metastatic breast cancer known to recruit abundant stroma[13].

[1]Department of Biomolecular Sciences, The Weizmann Institute of Science, Rehovot, Israel. [2]Department of Immunology, The Weizmann Institute of Science, Rehovot, Israel. [3]Chaim Sheba Medical Center, Cancer Research Center, Tel-Hashomer, Israel. [4]Department of Molecular Cell Biology, The Weizmann Institute of Science, Rehovot, Israel. [5]Pathology Institute, Tel-Hashomer, Israel. [6]Sackler Faculty of Medicine, Tel Aviv University, Tel Aviv, Israel. [7]Cancer Research UK Cambridge Institute, University of Cambridge, Cambridge, UK. [8]Department of Oncology, University of Cambridge, Cambridge, UK. [9]Breast Cancer Programme, Cancer Research UK Cancer Centre, Cambridge, UK. [10]Chaim Sheba Medical Center, Institute of Oncology, Tel-Hashomer, Israel. ✉e-mail: ido.amit@weizmann.ac.il; ruth.shouval@weizmann.ac.il

To avoid biases driven by a priori defined markers we used an index-sorting and negative-selection-based approach for isolation and massively parallel single-cell RNA-sequencing (MARS-seq) of CAFs[15]. We densely sampled cells along critical time points of tumor development, 2 weeks (2W) and 4 weeks (4W) after injection and from lung metastases (mets) spontaneously forming 4–5 weeks after primary tumor injection. Normal mammary fat pad fibroblasts (NMFs) from naive mice served as controls. Tumors or normal mammary fat pads were collected, dissociated into single-cell suspensions and live cells were stained with cell-surface markers: Ter119 (red blood cells), CD45 (immune) and EpCAM (epithelial) for negative selection; and podoplanin (PDPN; fibroblasts) for index sorting. All live cells negative for Ter119, CD45 and EpCAM were index sorted and single-cell processed by MARS-seq (Fig. 1a and Extended Data Fig. 1a). We analyzed 8,987 quality control (QC)-positive single cells from 12 tumor-bearing mice and 3 naive mice (Extended Data Fig. 1b,c and Supplementary Table 1) and used the MetaCell algorithm[16] to identify homogeneous and robust groups of cells ('metacells'), resulting in a detailed map of the 88 most transcriptionally distinct subpopulations (Supplementary Table 2). These metacells are organized into four broad classes: endothelial cells (characterized by expression of *Pecam1*), pericytes (*Rgs5*) and two classes of fibroblasts that we termed pCAFs (*Pdpn*) and sCAFs (*S100a4*; Extended Data Fig. 1d,e).

In silico, we removed *Pecam1* and *Rgs5* cells and a rare population (33 cells) negative for *Pecam1*, *Rgs5*, *Pdpn* and *S100a4* that highly expressed *Myc* and may have originated from cancer cells (see Methods). We continued our analysis with 3,875 *Pdpn* cells and 4,158 *S100a4* cells (Fig. 1b, Extended Data Fig. 1d,f and Supplementary Tables 3 and 4). Each of these fibroblast populations could be further divided into subsets with distinct transcriptional profiles (Fig. 1c) and differentially expressed genes (Fig. 1d), reproducible across mice and batches (Extended Data Fig. 1g). *Pdpn* fibroblasts expressed cell-surface PDPN protein (Fig. 1d lower panel) and included the NMF (*Gsn*) subset (Fig. 1e) and six subsets of pCAFs (Fig. 1f). Two of these expressed different gene modules involved in immune regulation and cell migration (*Cxcl12 and Saa3*); one had a wound-healing signature (*Acta2*; encoding for α-smooth muscle actin (α-SMA)); one had an extracellular fiber organization signature (*Fbn1*) and two had inflammatory signatures (*Cxcl1 and Il6*). *S100a4*-fibroblasts were devoid of NMFs and included two subsets of CAFs, albeit these subsets were not as clearly separated from each other as the pCAF subsets (Fig. 1d). One subset (*Spp1*$^{\mathrm{high}}$*S100A4*$^{\mathrm{low}}$) was enriched for signatures of antigen presentation (*H2-Aa*) and ECM remodeling (Fig. 1g). The other subset (*Spp1*$^{\mathrm{low}}$*S100A4*$^{\mathrm{high}}$) was enriched in protein-folding and metabolic genes (*Hspd1*; Fig. 1g).

To validate our single-cell sequencing results we performed bulk RNA-seq of sCAFs, pCAFs and NMFs and compared the profiles obtained by bulk and single-cell RNA-seq. All groups showed high correlation ($R > 0.5$) between bulk and cognate single-cell profiles (Extended Data Fig. 1h). The pCAF and NMF profiles also showed high correlation. The sCAFs, however, showed no correlation with pCAFs or NMFs (Extended Data Fig. 1h), suggesting that they have further diverged from NMF or perhaps have a different origin altogether. To exclude the potential contribution of cancer cells that have undergone epithelial-to-mesenchymal transition (EMT)[14] to the sCAF population, we analyzed the bulk RNA-seq data for lineage traces of 4T1 cancer cells (transfected plasmid reads; see Methods). This analysis confirmed that while some cancer cells may have escaped the negative-selection approach, the majority of sCAFs are derived from host mesenchymal cells (Supplementary Table 5; Methods).

CAF composition is dynamically reshaped as tumors progress and metastasize. Tumor heterogeneity increases with tumor progression[1,17,18]. Similarly, we and others have hypothesized that stromal heterogeneity increases as tumors progress. Accordingly, our analysis shows that metacell composition varies extensively between the different time points (Fig. 1d and Fig. 2a,b). Normal mammary fat pads harbored *Pdpn*$^+$ fibroblasts and were devoid of *S100a4*$^+$ fibroblasts. At 2W after tumor initiation, heterogeneity is observed: sCAFs constitute ~30% of the CAF population (Fig. 2b) and the majority express metabolic and protein-folding genes (*Hspd1*). The remaining ~70% of CAFs at 2W are *Pdpn*$^+$, yet in contrast to *Pdpn*$^+$ NMF, pCAFs are highly heterogeneous; more than half of them belong to the two immunoregulatory subpopulations (*Cxcl12* or *Saa3*), ~10% express ECM modules (*Fbn1*) and the remaining quarter exhibit a wound-healing profile (*Acta2*). At 4W after tumor initiation, the majority of CAFs are sCAFs (~77%), whereas only ~23% are pCAFs. Once again, the composition of metacells within each class has changed. The dominant pCAF populations at 4W are the wound-healing class (*Acta2*) and ECM-organizing pCAFs (*Fbn1*), whereas the immunoregulatory pCAF subpopulations (*Cxcl12; Saa3*) are diminished (Fig. 2b). The sCAF at 4W are composed largely of cells expressing ECM remodeling and antigen-presentation profiles (*Spp1* and *H2-Aa*). Lung mets contain mostly sCAFs (~70%) and share similar sCAF subpopulations with primary tumors (*Spp1 and H2-Aa*; *Hspd1*) at a 1:1 ratio. The pCAF population in mets (~30%) is comprised mostly of two inflammatory subpopulations (*Il6* and *Cxcl1*) that were not observed in primary tumors or in the normal mammary fat pad (Fig. 2b). The dynamic shift in CAF composition was confirmed by fluorescence-activated cell sorting (FACS) analysis of cell-surface PDPN protein expression. As tumors grew, the abundance of PDPN$^+$ cells within the stromal (CD45$^-$EpCAM$^-$) population decreased and the abundance of PDPN$^-$ cells increased (Extended Data Fig. 2a).

***Pdpn*$^+$ fibroblasts diverge into protumorigenic CAFs during tumor progression.** Different origins have been proposed for CAFs, including NMFs, MSCs and adipocytes[10–13]. Our metacell analysis showed that pCAFs (but not sCAFs) share similar patterns of transcription with NMFs (Fig. 1d and Extended Data Fig. 1h), suggesting that pCAFs may have originated from NMFs. To infer the most probable transcriptional trajectory for pCAFs we applied Slingshot, a computational method for cell lineage pseudo-time inference[19]. Slingshot analysis displayed a gradual transition from NMFs through early immunoregulatory and ECM-organizing pCAFs, to late immunoregulatory pCAFs, and eventually to wound-healing pCAFs (Fig. 2c,d). This trajectory is consistent with the transition from normal fibroblasts through 2W to 4W tumors (Extended Data Fig. 2b,c). NMFs expressed high levels of Hallmark genes encoding membrane bound and extracellular proteins (*Ppap2b*, *Ogn*, *Timp2* and *Igfbp6*). Expression of these genes gradually decreased along the trajectory leading to wound-healing pCAF (Fig. 2e, upper row and Extended Data Fig. 2d). In parallel, gradual increase in expression was observed for signature genes involved in cell migration and wound healing, such as *Timp1*, *Serpine1*, *Tpm1* and *Acta2* (Fig. 2e, lower row and Extended Data Fig. 2d). A third temporal pattern was genes whose expression was low in NMFs, high in the ECM/immunoregulatory pCAFs and low again in wound-healing pCAFs. These included *Cxcl12*, *Mmp3*, *Ccl7* and *Saa3* (Fig. 2e, middle row and Extended Data Fig. 2d).

sCAFs are transcriptionally distinct from pCAFs and NMFs. The sCAFs exhibit global gene-expression profiles that differ from those of pCAFs and NMFs (Extended Data Fig. 1f). Moreover, we could not find transitional cells linking these fibroblast types (Fig. 1d) that would suggest a gradual shift from NMFs to sCAFs, as observed for pCAFs. BM-derived MSCs are commonly viewed as a source of CAFs[10,20]. The molecular chaperone clusterin (*Clu*), was recently shown to play tumor-promoting

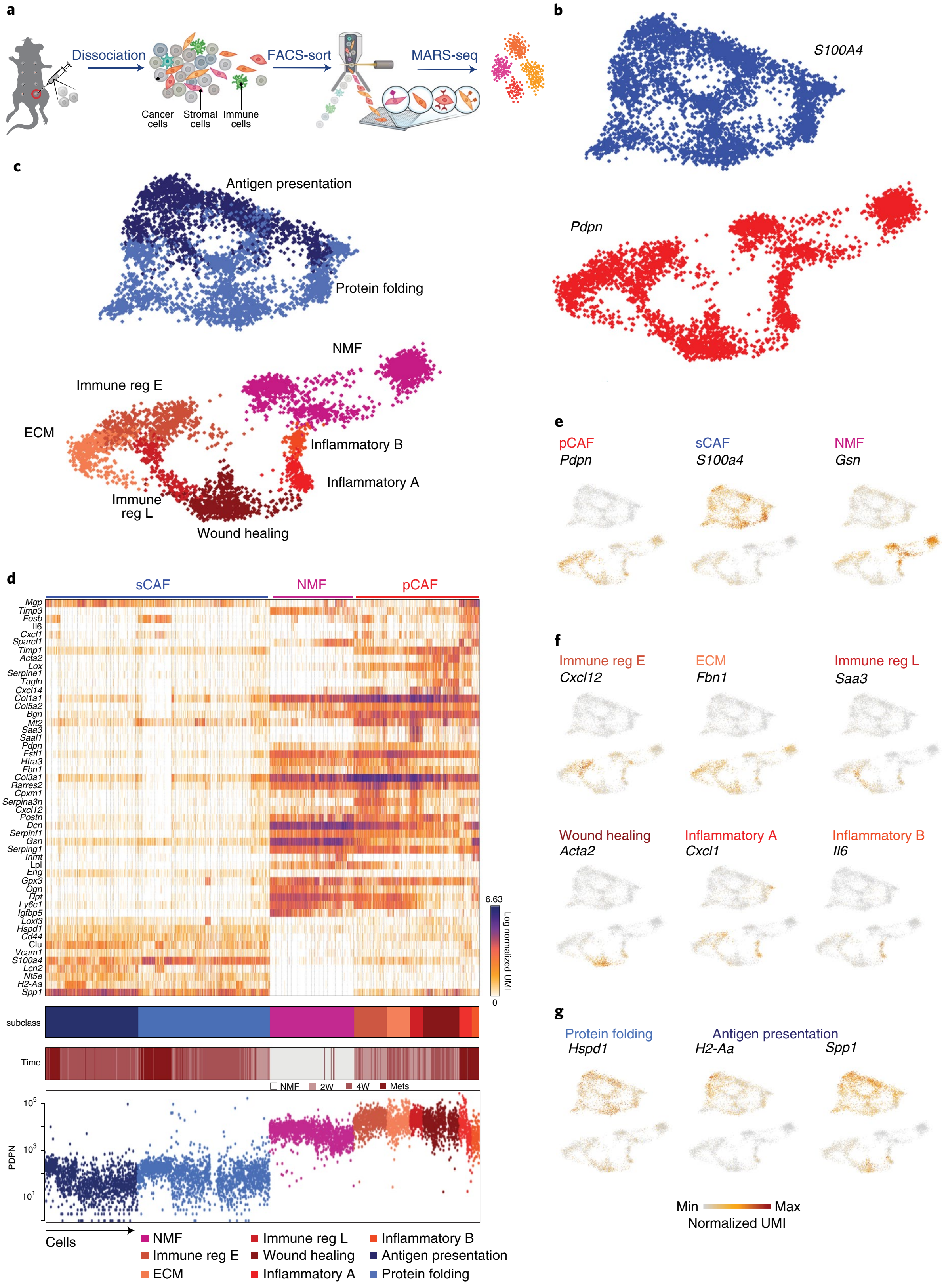

Fig. 1 | Breast CAFs consist of distinct subsets with diverse transcriptional profiles. **a**, Illustration of the experimental procedure. **b**,**c**, Single-cell RNA-seq data from CAF and NMF were analyzed and clustered using the MetaCell algorithm, resulting in a two-dimensional projection of 8,033 cells from 15 mice. The 83 metacells were associated with two broad fibroblast populations (**b**) and nine functional subclasses (**c**) annotated and color-coded. **d**, Gene expression of key marker genes across single cells from all subclasses of NMF, pCAF and sCAF. Lower panels indicate the association with subclass, the time point and the PDPN index sorting data, showing protein-level intensity in each cell. **e**–**g**, Expression of key marker genes for NMF, pCAF and sCAF (**e**); functional annotation for pCAF subclasses (**f**) and sCAF subclasses (**g**) on top of the two-dimensional projection of breast CAFs. Colors indicate log-transformed unique molecular identifier (UMI) counts normalized to total counts per cell.

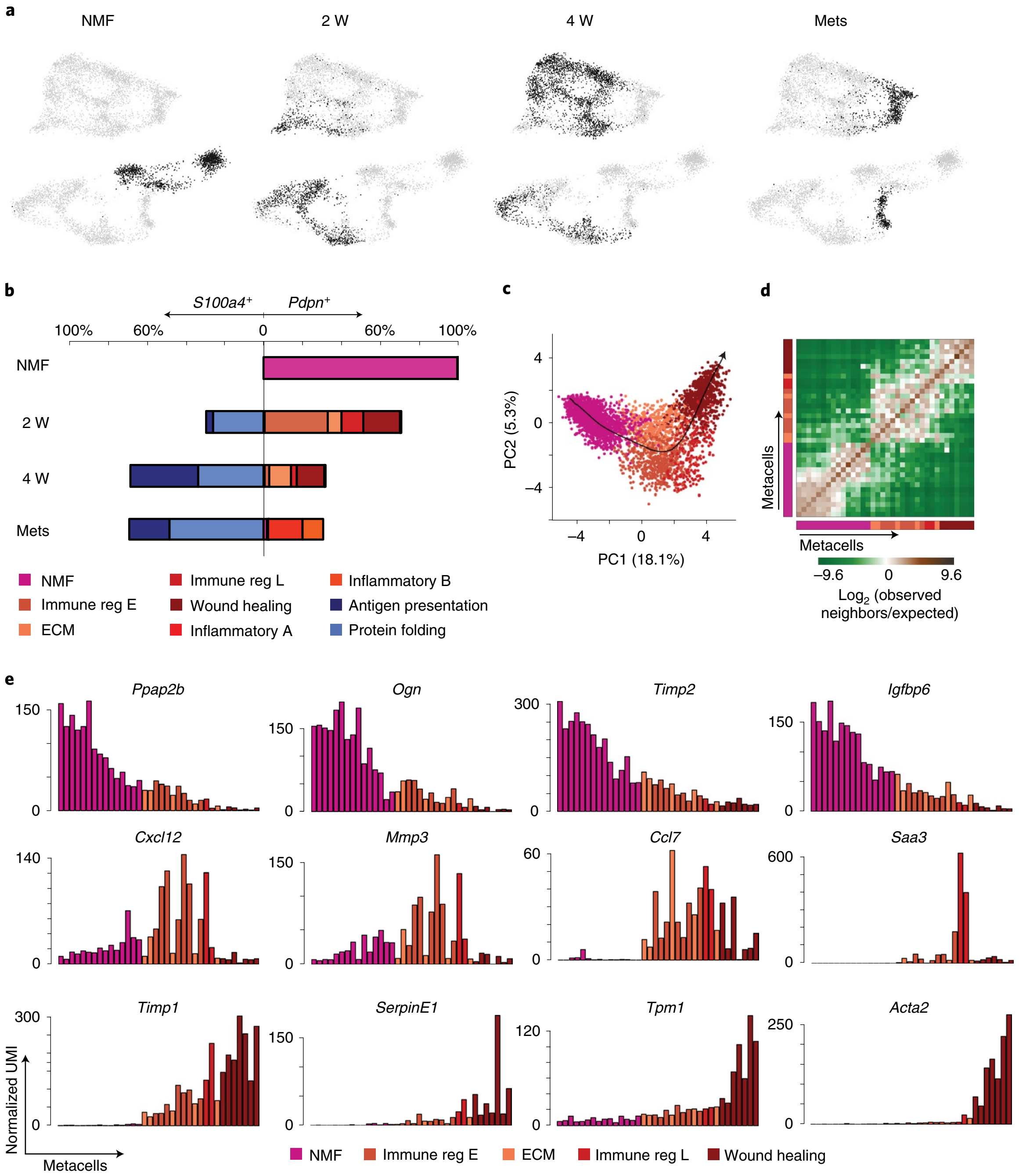

Fig. 2 | CAF composition and gene expression changes with tumor growth and metastasis. a, Projection of 8,033 cells from different time points (black) on top of the two-dimensional map of breast fibroblasts (presented in Fig. 1b,c). **b**, Compositions of *Pdpn*+ fibroblasts (right) and *S100a4*+ fibroblasts (left) at different time points (normalized to 100% total fibroblasts). Subclasses are annotated and color-coded. **c**–**e**, Slingshot analysis of pseudo-time trajectory from NMF to pCAF from 2W and 4W. A total of 3,465 cells were analyzed. Cells are color-coded as in **b**. **c**, Suggested trajectory from NMF to pCAF projected over the top two principal components. **d**, Heat map showing enrichment ($\log_2$ fold change) for *k*-nearest-neighbor connections between metacells over their expected distribution. Metacells are ordered by their position on the Slingshot pseudo-time. **e**, Expression of Hallmark NMF and pCAF genes across metacells (average UMI per cell), ordered by pseudo-time.

roles in BM-MSC-derived CAFs recruited to breast tumors in mice[10]. Indeed, *Clu*, as well as several other MSC markers (*Vcam1*, *Cd44*, *Eng* and *Nt5e*), were differentially upregulated in sCAFs compared to pCAFs (Fig. 1d and Fig. 3a). Together with the observation that *S100a4*+ fibroblasts are not found in the normal mammary fat pad, this suggests that sCAFs arise from a different origin than pCAFs and are recruited to the tumor, perhaps from BM-MSCs.

sCAFs show a continuum of cell states bounded by four major transcriptional programs. Unlike pCAFs, sCAFs do not seem to form discrete subpopulations, but rather a continuum in gene-expression space, implying a continuum of cell states. To infer biological functions associated with these cell states, we applied the Pareto task inference (ParTI) method[21,22]. ParTI is based on an evolutionary theory suggesting that when cells need to perform multiple functions, no single gene-expression profile can be optimal

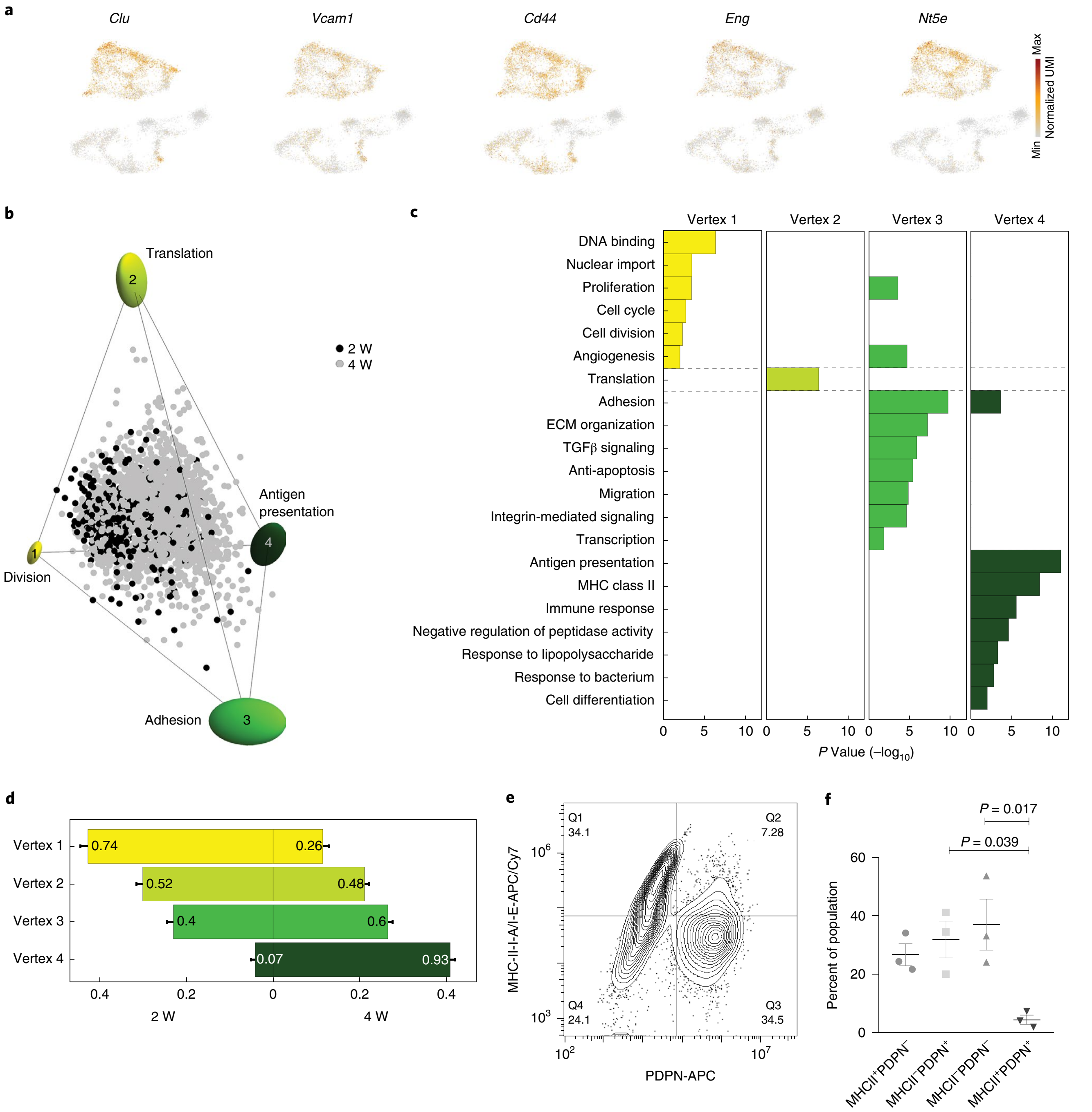

Fig. 3 | sCAFs show a continuum of cell states which fills a tetrahedron in gene-expression space, suggesting a tradeoff between four functions. a, Expression of Hallmark MSC marker genes on top of the two-dimensional projection of breast cancer stroma (presented in Fig. 1b,c), in a total of $n = 8{,}033$ cells from 15 mice. Colors indicate log-transformed UMI counts normalized to total counts per cell. **b**, ParTI analysis of 2W and 4W sCAF single-cell gene expression in the space of the first three principal components shows a continuum that can be well enclosed by a tetrahedron. At the vertices are ellipses that indicate s.d. of vertex position from bootstrapping. Cells are color-coded according to time point. Vertices are annotated and color-coded, $n = 2{,}292$ cells. **c**, Gene ontology (GO) enrichment in the different vertices (see full list in Supplementary Table 6), $n = 2{,}292$ cells. Gene enrichment was calculated by Spearman rank correlation between the gene's expression and the Euclidean distance of cells from the vertex, as detailed in Methods. TGF, transforming growth factor. **d**, Relative representation of each time point in the four vertices. The x axis shows the fraction of cells from 2W and 4W closest to each vertex. Numbers in the bars are the fraction of each time point in the 100 cells closest to each archetype. **e**,**f**, Flow cytometry analysis of cell-surface expression of MHC-II molecules I-A/I-E versus PDPN in CD45$^-$EpCAM$^-$ cells from 4W tumors. A representative flow cytometry plot is shown in **e**, quantification of results is presented in **f**, $n = 3$ mice, mean ± s.e.m. P values were calculated using one-way analysis of variance (ANOVA) followed by Tukey's multiple comparisons test.

for all functions at once. This tradeoff leads to specific patterns in the data: individual cells fall into a polyhedron in gene-expression space[22]. Cells near a vertex are specialists at a particular function, whereas cells near the middle of the polyhedron are generalists[22,23]. We first applied ParTI on NMFs, 2W and 4W CAFs. Mets clustered separately in this analysis and were therefore excluded (see

Methods). The pCAFs clustered with NMFs and sCAFs formed a distinct cluster, confirming our metacell analysis (Extended Data Fig. 3a). Next we analyzed each cluster separately. pCAFs and NMFs formed a one-dimensional continuum (curve) in agreement with the Slingshot analysis (Extended Data Fig. 3b). The sCAF gene expression could not be explained well by a one-dimensional continuum (curve) or a two-dimensional planar polygon (Extended Data Fig. 3c). Rather, sCAF transcriptional states were best described as a continuum in a tetrahedron (Fig. 3b and Extended Data Fig. 3d–i). At the vertices of this tetrahedron are four transcriptional programs representing distinct biological functions (Fig. 3b and Extended Data Fig. 3d). Vertex 1 is enriched with cells expressing programs for cell division and proliferation (Fig. 3c and Supplementary Table 6). Vertex 2 corresponds to protein translation, vertex 3 to adhesion, ECM-organization, prosurvival and migration programs and vertex 4 to immune response programs, in particular antigen presentation via major histocompatibility class (MHC) class II genes (Fig. 3c and Supplementary Table 6). The distribution of cells within the tetrahedron changed with tumor growth (Fig. 3d). The sCAFs in 2W tumors were located mostly in the space between vertices 1–3, indicating that they express transcriptional programs of division, adhesion and protein translation (Fig. 3d). Antigen-presentation programs were expressed mostly by 4W sCAFs and scarcely by 2W sCAFs, suggesting a temporally dynamic division of functions between sCAFs in breast tumors.

We further tested expression of MHC class II using flow cytometry analysis of sCAFs and pCAFs from 4W tumors. The MHC class II cell-surface molecules I-A/I-E$^+$ were expressed by ~50% of 4W sCAFs, but not by pCAFs (Fig. 3e,f).

PDPN and S100A4 mark mutually exclusive, morphologically distinct CAFs in mouse breast tumors. To validate our classification and examine the spatial distribution of the CAF subpopulations, we performed immunohistochemical staining of 4T1 tumors from different stages with anti-S100A4 and anti-PDPN. Cytokeratin (CK) was used to identify cancer cells. NMFs showed very weak expression of S100A4, whereas PDPN$^+$ fibroblasts were abundant (Fig. 4a, upper panel). The 2W and 4W tumors harbored both PDPN$^+$ and S100A4$^+$ cells. The expression pattern of both proteins was different than that of CK, suggesting that these are stromal cells (Fig. 4a, middle panels). Mets were rich in S100A4$^+$ cells (Fig. 4a, lower panel). PDPN was scarcely expressed in mets and strongly expressed in the normal adjacent lung tissue (Fig. 4a, lower panel). At all tumor stages, pCAFs were long and spindly, resembling the morphology of NMFs and sCAFs were smaller. Both classes of CAFs were distributed in all regions of the tumor (Fig. 4a).

Multiplexed immunofluorescent (MxIF) staining confirmed that S100A4 and PDPN mark different populations of cells (Fig. 4b and Extended Data Fig. 4). We saw partial overlap between S100A4 and CK staining, mostly in normal mammary fat pads (Extended Data Fig. 4a,c). Nevertheless, the majority of S100A4 cells in primary tumors and in metastases were CK$^-$, confirming our sequencing results and suggesting that PDPN$^+$ cells and S100A4$^+$ cells are distinct subtypes of CAFs (Fig. 4b and Extended Data Fig. 4).

To test the robustness of our CAF classification we used a different mouse model of TNBC (E0771 cancer cells orthotopically injected into the mammary fat pad of immunocompetent C57BL/6 mice). MxIF staining of 4W tumors showed that, similarly to the 4T1 model, S100A4 and PDPN mark distinct populations of CAFs in E0771 tumors. Neither PDPN nor S100A4 overlapped with CK$^+$ cancer cells (Extended Data Fig. 5a–c).

Ly6C$^+$ pCAFs are immunosuppressive. Our sequencing results suggested that pCAFs consist of diverse subpopulations performing distinct tasks such as immune regulation and wound healing. To test the functional relevance of these findings we first performed flow cytometry to define markers for the pCAF subpopulations. We stained pCAFs from primary 4T1 and E0771 tumors with antibodies against Ly6C as a marker for the immunoregulatory subpopulation and α-SMA (encoded by *Acta2*) as a marker for the wound-healing subpopulation (Fig. 1d). These proteins marked distinct subpopulations of cells (Fig. 5a and Extended Data Fig. 5d). The Ly6C$^+$α-SMA$^-$ subpopulation was most abundant in NMFs and decreased as tumors progressed, whereas the Ly6C$^-$α-SMA$^+$ subpopulation was lowest in NMFs and increased as tumors progressed (Fig. 5b), similarly to a Ly6C$^-$α-SMA$^-$ subpopulation.

Because Ly6C$^+$ pCAFs in the primary tumor expressed an immunoregulatory module we next examined their potential to suppress T-cell proliferation in vitro. We activated CD8$^+$ T cells by CD3/CD28 beads, in the presence of Ly6C$^+$ or Ly6C$^-$ pCAFs isolated from 4T1 primary tumors and measured their proliferation after 48 h of co-culture by carboxyfluorescein succinimidyl ester (CFSE) staining (Fig. 5c,d). We found a significant difference in the effect of these two pCAF subpopulations on activated CD8$^+$ T-cell proliferation: while Ly6C$^-$ pCAFs had no effect on T-cell proliferation (when normalized to monoculture of activated T cells without CAFs; Fig. 5d), Ly6C$^+$ pCAFs caused a 1.5-fold reduction in CD3/CD28-mediated CD8$^+$ T-cell proliferation (Fig. 5d). The suppression of T-cell proliferation was accompanied by a significant reduction in CD8$^+$ T-cell activation, as measured by the increase in CD25 and CD69 activation markers in CD8$^+$ T cells grown in co-culture with Ly6C$^+$ but not with Ly6C$^-$ pCAFs (Fig. 5e). These results support our molecular profiling results and suggest that Ly6C$^+$α-SMA$^-$ pCAFs suppress CD8$^+$ T-cell activation and proliferation, whereas Ly6C$^-$ pCAFs do not.

To test whether Ly6C$^-$ pCAFs exhibit wound-healing functions, we examined their ability to secrete collagen in vitro using Sirius Red staining (Methods). We found that Ly6C$^-$ pCAFs secreted significantly more collagen than Ly6C$^+$ pCAFs, further supporting the transcriptional profiling results, and suggesting that Ly6C$^-$ pCAFs may have wound-healing functions (Fig. 5f,g).

S100A4 and PDPN mark distinct stromal populations in human breast tumors. To test the clinical relevance of our findings, we performed MxIF staining for PDPN and S100A4 in human estrogen receptor positive (ER$^+$) breast cancer and TNBC tissue samples. CK staining was performed to mark epithelial cancer cells (Fig. 6a). We found that PDPN$^+$ cells and S100A4$^+$ cells are major constituents of human breast cancer stroma and exhibited very low overlap with CK staining (Fig. 6a,b and Extended Data Fig. 6a,b). A minor overlap was observed between S100A4 and CD45 staining, in cells with mesenchymal morphology (Extended Data Fig. 6c). Similarly to our mouse models, PDPN$^+$ cells and

Fig. 4 | PDPN and S100A4 proteins are expressed on distinct types of breast CAFs in mouse tumors. a, Consecutive formalin-fixed paraffin-embedded (FFPE) tissue sections of tumors, mets or normal mammary fat pads were immunostained with antibodies against the indicated proteins or stained with hematoxylin & eosin (H&E), *n* = 3 mice per time point. Representative images are shown. All images were collected at the same magnification and are presented at the same size. Scale bar, 100 μm. For each panel, regions marked by rectangles are shown as 2.5× insets in black dashed rectangles. A dashed red line on the H&E marks the metastatic region in the lung. **b**, MxIF staining was performed with antibodies against the indicated proteins, *n* = 3 mice per time point. Representative images of 2W and 4W tumor FFPE sections are shown. Scale bar, 50 μm, inset scale bar, 17 μm. DAPI, 4,6-diamidino-2-phenylindole.

S100A4$^+$ cells were mutually exclusive (Fig. 6b). These observations suggest that PDPN and S100A4 mark distinct subtypes of CAFs in human breast tumors.

We observed partial segregation in the spatial organization of CAFs in human tumors (Fig. 6a). Both in ER$^+$ and TN samples, a subset of pCAF was found immediately adjacent to CK$^+$ cancer cells

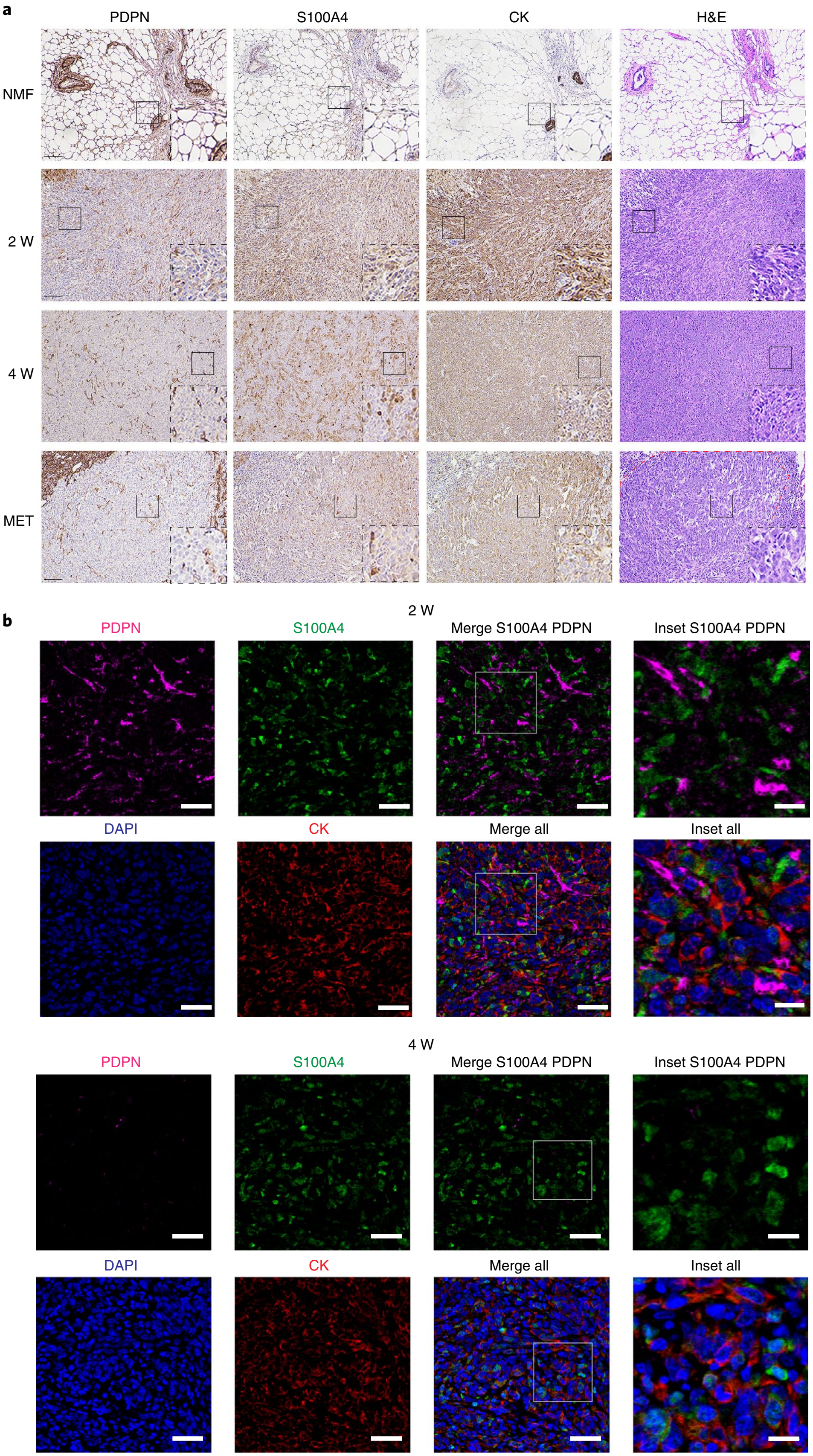

or infiltrating the cancerous region. The rest of the pCAFs were dispersed in stromal regions, mixed with sCAFs. In contrast, sCAFs were less frequently found immediately adjacent to cancer cells (Fig. 6a, insets).

A subset of human sCAFs expresses MHC class II, whereas a subset of pCAFs expresses α-SMA. To further characterize human sCAFs and pCAFs, we tested several of the markers for sCAF and pCAF subpopulations found in our single-cell RNA-seq data by MxIF in a small cohort of patients with TNBC. α-SMA was widely expressed by pCAFs but not by sCAFs (Fig. 6c,e,f and Extended Data Fig. 6b). The MHC class II cell-surface receptor HLA-DR marked a subset of sCAFs (Fig. 6c–e and Extended Data Fig. 6a), but not pCAFs. NT5E (aka CD73) localized to subsets of sCAFs as well as pCAFs (Fig. 6c–e and Extended Data Fig. 6a). These results support our findings from the 4T1 murine model and provide combinations of markers to detect distinct CAF subpopulations in human patients.

S100A4/PDPN ratio is correlated with disease outcome in two independent cohorts of patients with breast cancer. To study the clinical significance of these findings, we co-stained and scored PDPN, S100A4 and CK immunostaining in a cohort of 72 patients with TNBC with long-term clinical follow up (Supplementary Table 7). For each patient, we stained three cores of the tumor, calculated the average area of positive staining for each marker (Fig. 7a), as well as ratios between the three markers and evaluated whether the staining scores correlate with each other (Extended Data Fig. 7a) and with disease outcome. High CK expression led to increased hazard of recurrence, as expected and significantly correlated with poor survival ($P=0.028$; Supplementary Table 8). Next we evaluated our stromal markers. PDPN levels significantly correlated with disease outcome ($P=0.013$; Supplementary Table 8); patients whose tumors had high PDPN levels had shorter recurrence-free survival ($P=0.026$; Fig. 7b), as well as overall survival ($P=0.0011$; Extended Data Fig. 7b). S100A4 on its own was not significantly correlated with disease outcome in this cohort, yet its hazard ratio value was smaller than 1 (while the hazard ratio of PDPN was greater than 1; Supplementary Table 8). We therefore asked whether evaluation of the S100A4/PDPN ratio could improve our ability to predict patient outcome. Indeed, we observed a striking correlation between high S100A4/PDPN ratios and increased recurrence-free survival ($P=0.0032$) and overall survival ($P=0.00015$; Fig. 7c and Extended Data Fig. 7c).

To test for possible correlation between S100A4/PDPN ratio and T-cell infiltration we stained and scored CD3 (Extended Data Fig. 8a,b). We found no significant correlation between CD3 and disease outcome (Supplementary Table 8), nor did CD3 staining correlate with any of the other cell markers tested (Extended Data Fig. 7a).

To quantitatively test the observation that pCAFs infiltrate the cancerous region more than sCAFs we defined regions of dense stroma versus cancer-adjacent regions based on CK staining and calculated the average area of positive staining for S100A4 and PDPN in each region (Extended Data Fig. 7d). The pCAFs were ~3-times more abundant in cancer-adjacent regions than in dense stroma regions (Fig. 7d and Extended Data Fig. 7e). The sCAFs infiltrated the cancerous region significantly less than pCAFs and the average ratio of cancer-adjacent S100A4/dense-stromal S100A4 was 0.8 (Fig. 7d and Extended Data Fig. 7e).

Our initial observation that S100A4 and PDPN stain not only TNBC but also ER^+ breast cancer samples suggested that S100A4/PDPN ratio may be a general marker of disease outcome in breast cancer. To test this we stained and scored PDPN, S100A4 and CK in an independent cohort of 293 patients with breast cancer from the METABRIC study[24] (Supplementary Table 9). In this cohort of mixed breast cancer subtypes, S100A4/PDPN ratios significantly correlated with disease progression ($P=0.025$; Fig. 7e). Similarly to the TNBC cohort, high S100A4/PDPN ratios were associated with increased recurrence-free survival in the METABRIC cohort (Fig. 7e). The spatial distribution of sCAFs and pCAFs was also similar in the two cohorts, with higher average cancer-adjacent PDPN/dense-stromal PDPN than cancer-adjacent S100A4/dense-stromal S100A4 (Extended Data Fig. 7f,g).

High S100A4/PDPN ratios are associated with *BRCA* mutations in TNBC. A substantial fraction of patients with TNBC carry mutations in *BRCA* genes, in particular *BRCA1* (ref. [25]) and *BRCA* mutations frequently lead to TNBC[26]. While the METABRIC cohort had very few patients with *BRCA* mutations, in the TNBC cohort, 20 of 45 patients (with documented *BRCA* status) carried such mutations (Supplementary Tables 7 and 9). These patients exhibited increased T-cell infiltration (measured by CD3 staining) compared to patients with wild-type *BRCA* (Extended Data Fig. 8c), yet neither T-cell infiltration nor *BRCA* status correlated with survival (Extended Data Fig. 8d and Supplementary Tables 8 and 10).

We therefore tested for possible associations between *BRCA* status, CAF marker expression and survival (Fig. 8a–c and Extended Data Fig. 8b). PDPN levels and S100A4/PDPN ratio significantly correlated with *BRCA1/2* mutational status (Fig. 8b,c). Patients with mutant *BRCA1/2* exhibited significantly lower PDPN staining and higher S100A4/PDPN ratios compared to *BRCA* wild-type patients (Fig. 8b,c). Moreover, multivariate Cox regression analysis of recurrence-free survival, considering S100A4/PDPN ratio and *BRCA* mutational status showed a strong interaction between the two parameters (Supplementary Table 10). Indeed, when stratified according to *BRCA* status as well as S100A4/PDPN ratio a clear

Fig. 5 | $Ly6C^+$ pCAFs suppress $CD8^+$ T-cell proliferation, in vitro. a,**b**, FACS analysis of Ly6C and α-SMA expression in $CD45^-EpCAM^-PDPN^+$ cells freshly collected from normal mammary fat pads, 2W tumors and 4W tumors and immediately fixed. Representative flow cytometry plots from one mouse are shown in **a** and the results are quantified in **b**, $n=6$ mice for NMF and 2W; $n=8$ mice for 4W. Data are combined from three independent experiments and are presented as mean and analyzed using two-way ANOVA followed by Tukey's multiple comparisons test. P_{int} – P interaction between time and population. **c**,**d**, $CD45^-EpCAM^-PDPN^+$ cells from 4W tumors were sorted to $Ly6C^+$ versus $Ly6C^-$ populations, which were then incubated in vitro at a 1:1 ratio with $CD8^+$ T cells activated by CD3/CD28 beads and marked by CFSE for 48 h. Representative FACS plots of CFSE signals from one experiment are shown in **c** and the results from $n=5$ independent experiments, each with different mice, normalized to the average proliferation with no CAFs per experiment are presented in **d** as mean ± s.d., analyzed utilizing a two-sided Student's *t*-test. **e**, Flow cytometry analysis of CD25 and CD69 activation markers in $CD8^+$ T cells activated and co-cultured with pCAFs as described in **c** or incubated in monoculture with and without activation. The experiment was repeated three times, each with different mice. Results from one representative experiment are shown in **e**. For nonactivated $CD8^+$ and activated $CD8^+$, $n=3$; for activated $CD8^+$ with $Ly6C^+$ CAFs, $n=4$; for activated $CD8^+$ with $Ly6C^-$ CAFs, $n=5$ independent culture wells; mean ± s.e.m. are shown and data were analyzed by two-way ANOVA followed by Tukey's multiple comparisons test. **f**,**g**, $CD45^-EpCAM^-PDPN^+$ cells from 4W 4T1 tumors were sorted to $Ly6C^+$ versus $Ly6C^-$ populations, which were then grown to confluence in vitro, passaged once, allowed to secrete collagen for 4 d and stained with Sirius Red (see Methods). The experiment was repeated four times, each with different mice. Results from one representative experiment are shown in **f**. Quantification of Sirius Red staining in a representative experiment is shown in **g**, $n=4$ $Ly6C^+$; $n=3$ $Ly6C^-$ independent culture wells. Mean ± s.e.m. is shown and data were analyzed by a two tailed Student's *t*-test. Scale bar, 500 μm, inset scale bar, 250 μm.

separation appeared; the S100A4/PDPN ratio was a significant classifier of recurrence-free survival in carriers of *BRCA* mutations, but not in patients with wild-type *BRCA* (Fig. 8d).

Discussion

Intratumor heterogeneity is a critical driver of tumor evolution and the main source of therapeutic resistance[18,27,28]. Our understanding

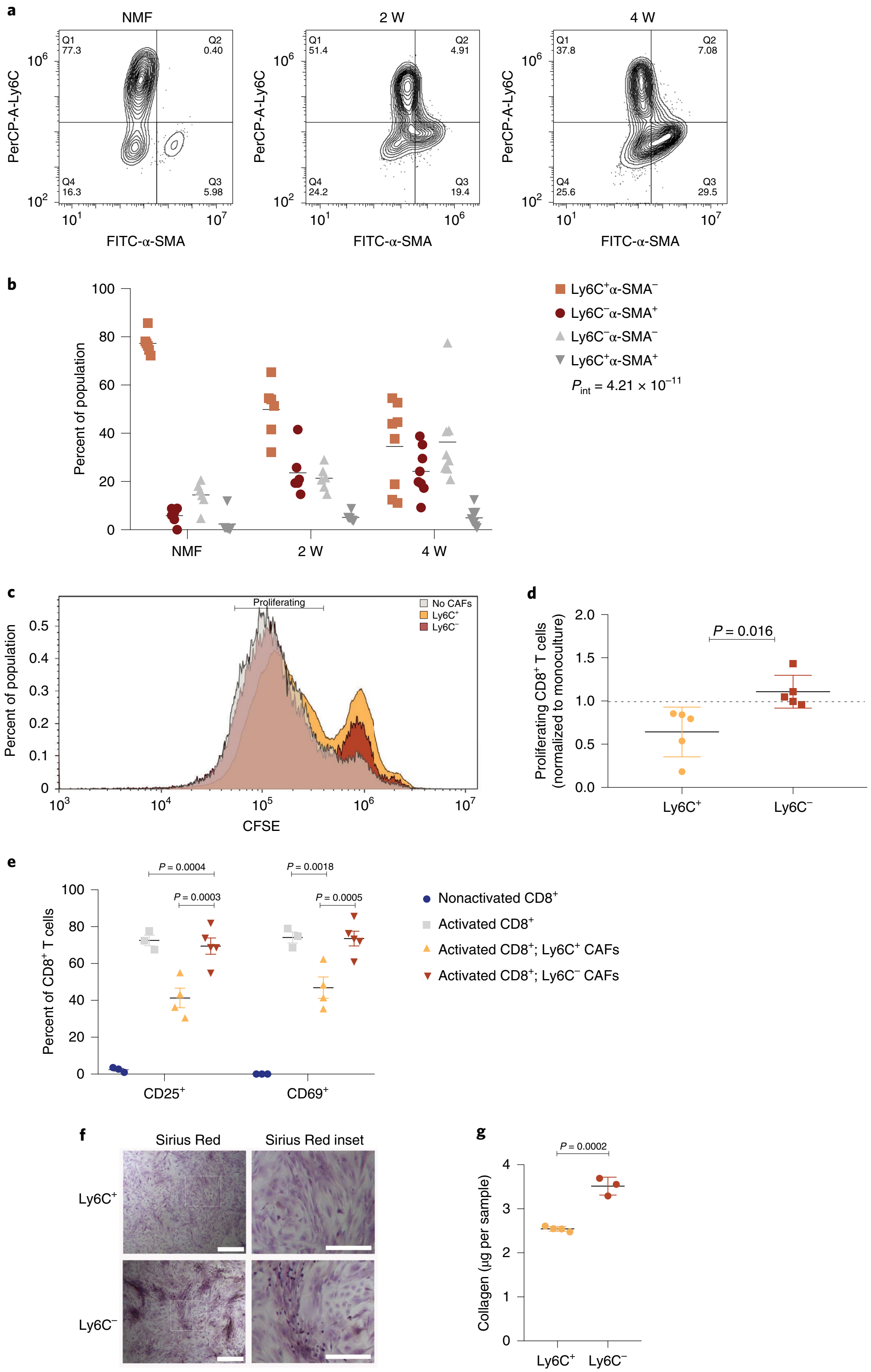

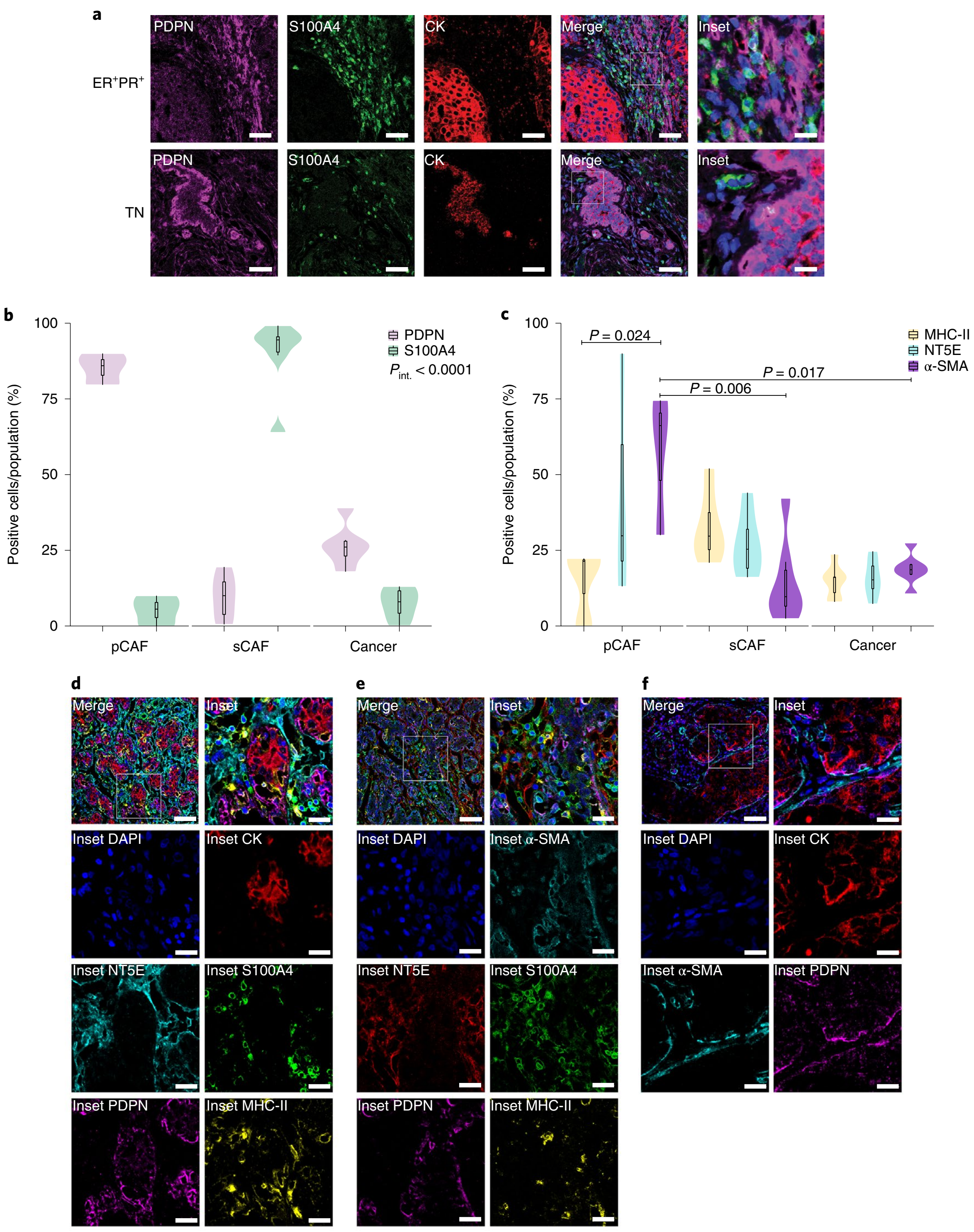

Fig. 6 | PDPN and S100A4 mark distinct populations of CAFs in human breast cancer. a, MxIF staining of FFPE tissue sections from patients with ER$^+$ breast cancer or TNBC with antibodies against the indicated proteins. Staining was performed on five patients with ER$^+$ and six patients with TNBC. Representative images from a patient with ER$^+$PR$^+$HER2$^-$ and TNBC are shown, $n = 11$ patients, combined from two independent experiments. Scale bar, 50 μm; inset scale bar, 12.5 μm. PR, progesterone receptor. **b–f**, FFPE tumor sections from 12 patients with TNBC were MxIF stained with antibodies against the indicated proteins. Cells were classified using QuPath (see Methods) to pCAFs, sCAFs or cancer cells based on PDPN, S100A4 and CK staining (**b**) and the expression of MHC-II, NT5E and α-SMA in each class was determined (**c**), $n = 3$ patients for pCAF; $n = 6$ patients for sCAF and cancer. Median is presented with first and third quartiles, with trimmed violin plot overlay. Probability comparisons were performed using two-way ANOVA (**b**,**c**) with Tukey correction for multiple comparisons in **c**. P value of the interaction of cell and marker (P_{int}) is shown in **b**. Representative merged images and insets of the independent channels are shown in **d–f,** $n = 8$ patients for **d**; $n = 6$ patients for **e**; $n = 5$ patients for **f**. Scale bar, 50 μm; inset scale bar, 17 μm.

of how the TME and in particular CAFs, contribute to this heterogeneity is still lacking. Here we find that breast CAFs consist of diverse subpopulations that change over the course of tumor growth and metastasis. These subpopulations cluster into two prototype CAF subtypes, which we term pCAF and sCAF, based on mutually exclusive expression of PDPN in pCAFs and S100A4 in sCAFs.

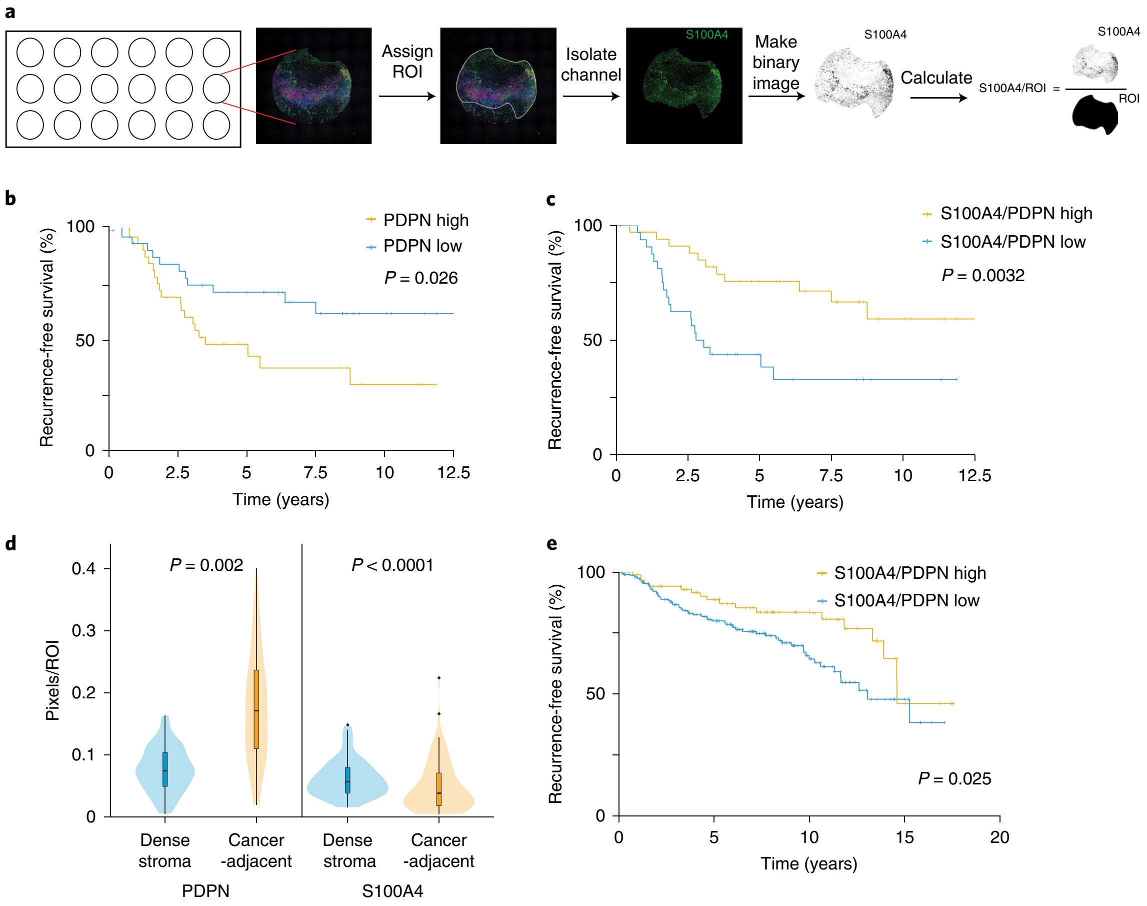

Fig. 7 | PDPN and S100A4 stromal staining is correlated with disease outcome in human patients with breast cancer. a, Illustration of pixel-based image analysis workflow. ROI, region of interest. **b**,**c**, FFPE tumor microarray (TMA) sections from a cohort of patients with TNBC ($n = 70$) were immunostained for PDPN, S100A4 and CK and scored (see Methods). PDPN scores (**b**) or S100A4/PDPN scores (**c**) were classified as higher or lower than the median and the association with recurrence-free survival of $n = 70$ patients was assessed by Kaplan–Meier analysis. *P* value was calculated using log-rank test (two sided). **d**, Cancer-adjacent regions and regions of dense stroma were determined for each core in the TNBC TMA based on CK staining (see Methods) and PDPN and S100A4 staining in each region was scored, $n = 70$ patients and median is presented with first and third quartiles with trimmed violin plot overlay. *P* value was calculated using a two-sided Wilcoxon matched pairs signed-rank test. **e**, FFPE TMA sections of patients with breast cancer from the METABRIC cohort ($n = 288$ patients) were stained and scored for PDPN, S100A4 and CK as described in **b**,**c**. S100A4/PDPN scores were classified as higher ($n = 88$) or lower ($n = 200$) than 1 (five outlier samples were omitted from the analysis; see Methods) and the association with recurrence-free survival was assessed by Kaplan–Meier analysis. *P* value was calculated using a two-sided log-rank test.

Establishing the relevance of our experimental findings to human disease, pCAFs and sCAFs are major constituents of human breast cancer stroma and the ratio of S100A4/PDPN expression is a classifier of disease outcome in two independent cohorts of patients.

Recent studies used RNA-seq approaches to characterize the TME in different types of cancer[10,14,29–33]. In pancreatic cancer, two spatially separated and reversible subtypes of CAFs have been identified, myofibroblasts (myCAFs), located immediately adjacent to cancer cells and inflammatory fibroblasts (iCAFs), located within the dense pancreatic tumor stroma[32]. In breast cancer, a population of matrix remodeling CAFs similar to myCAF was identified and termed mCAFs[14]. Recently, a third population of pancreatic CAFs, antigen-presenting CAFs (apCAFs) was identified[30]. Both myCAF and iCAF share similarities with subpopulations of the pCAFs that we have identified. In particular, iCAFs share common genes with the inflammatory subpopulations of pCAFs (*Cxcl1*, *Il6*), and myCAFs are similar to wound-healing pCAFs (*Acta2*). In agreement with our analysis suggesting that pCAFs originate from tissue-resident fibroblasts, both myCAFs and iCAFs can be derived from tissue-resident pancreatic stellate cells. The apCAFs, on the other hand, share common genes with sCAFs, in particular with the antigen-presenting sCAFs (*H2-Ab1*, *CD74*, *Slpi*), suggesting that these CAFs may serve similar roles in different tumor types[30].

In breast cancer, CAFs were recently classified into four subclasses with different spatial localization based on a predefined set of cell-surface markers[9]. CAF-S3 in that report were S100A4$^{\mathrm{High}}$α-SMA$^{\mathrm{low}}$, and localized away from cancer cells, as opposed to CAF-S4 which were S100A4$^{\mathrm{Low}}$α-SMA$^{\mathrm{High}}$ and localized closer to cancer cells[9]. CAF-S3 in that study was not molecularly analyzed; however, the localization further away from cancer cells (compared to S100A4$^{\mathrm{Low}}$α-SMA$^{\mathrm{High}}$ CAF) may suggest similarities between CAF-S3 and sCAFs. Another report identified S100A4$^{\mathrm{High}}$α-SMA$^{\mathrm{low}}$ CAFs originating from tissue-resident adipocytes[12]. While those CAFs do not share a common morphology or common molecular characteristics with the sCAFs identified here, both reports highlight the possibility that CAFs originate from cells other than tissue-resident fibroblasts.

Indeed, CAFs have heterogeneous origins[10–14]. Three distinct computational approaches (MetaCell, Slingshot and ParTI) point to NMF as the most probable origin of pCAFs. The origin of sCAFs

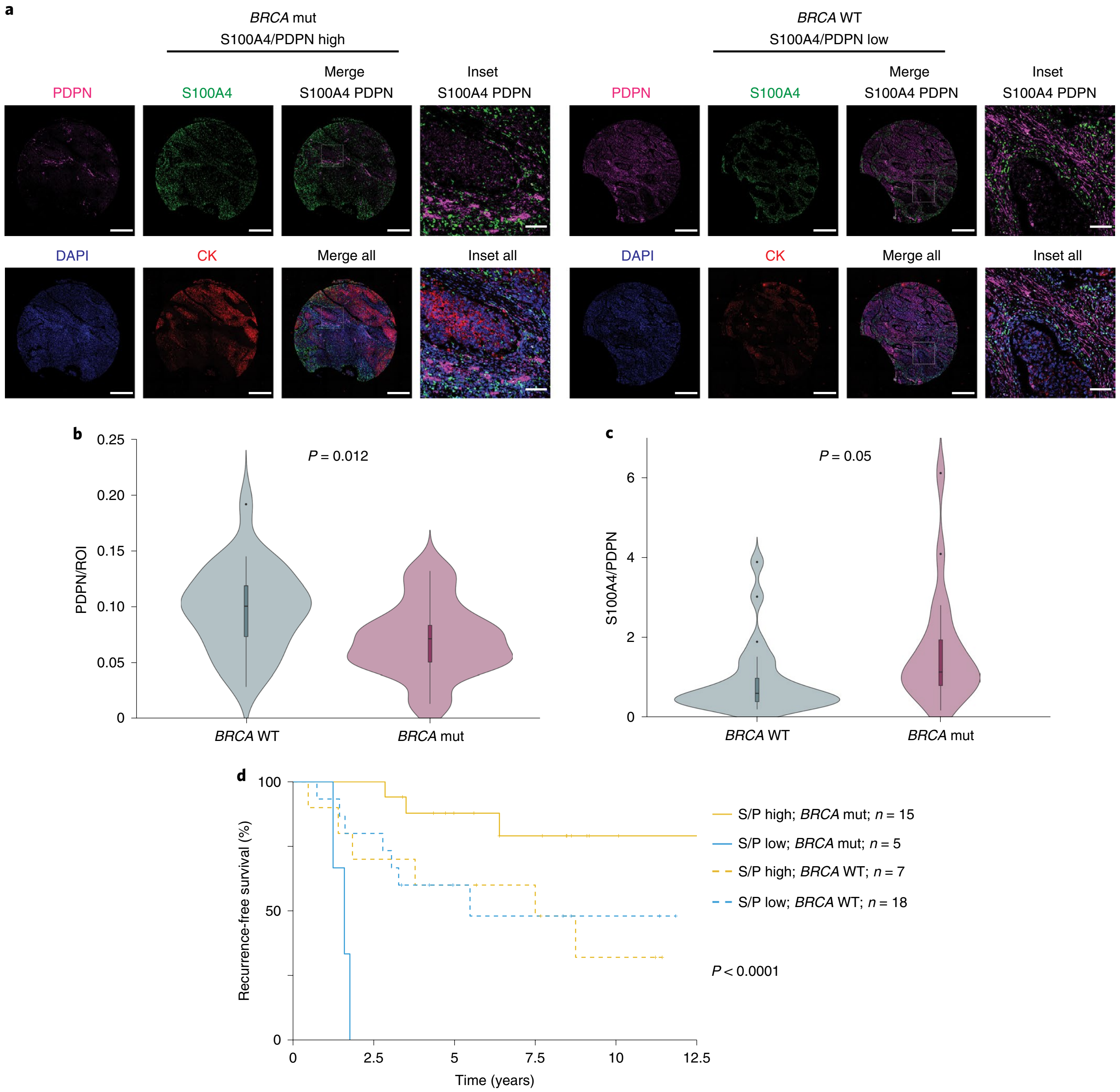

Fig. 8 | S100A4/PDPN ratio is a classifier of recurrence-free survival in *BRCA*-mutated TNBC. a, Representative images of PDPN, S100A4, CK and DAPI staining in a patient with *BRCA* mutation (mut) and a patient with wild-type (WT) *BRCA* from our cohort of 72 patients with TNBC. Scale bar, 500 µm; inset scale bar, 80 µm. **b**,**c**, Untrimmed vase box plots depicting PDPN (**b**) or S100A4/PDPN (**c**) staining scores (see Methods) in patients with *BRCA* WT ($n = 25$) versus *BRCA* mut ($n = 20$) from the TNBC cohort. Median is presented with first and third quartiles, with untrimmed violin plot overlay. *P* value was calculated using a two-sided Student's *t*-test. **d**, Multivariate analysis through Cox proportional hazard regression model for the TNBC data was performed, then patients with TNBC were stratified by *BRCA* mutational status and the association of S100A4/PDPN scores (higher versus lower than median) with recurrence-free survival was assessed by Kaplan–Meier analysis. *P* value for the model was calculated using two-sided log-rank test.

is less clear. While we cannot rule out the possibility that sCAFs originate from NMFs, this is unlikely because their transcriptional makeup is disconnected. It is also unlikely that sCAFs originated from cancer cells that have undergone EMT, though a minority of cancer cells may have escaped through the negative-selection sequencing approach. Rather, we postulate that sCAFs originate from a different mesenchymal source, perhaps BM-MSCs[10,34,35]. The sCAFs are enriched for several classic MSC markers. Moreover, *Clu*, recently reported to play a tumor-promoting role in BM-MSC-derived CAFs[10], is among the most differentially upregulated genes in sCAFs (compared to pCAFs). These findings support the hypothesis that sCAFs are derived from MSCs that are recruited to the tumor and differentiate into CAFs. In the tumor, sCAFs dynamically shift between several transcriptional programs; cell division, protein translation and adhesion are expressed in early tumors. As tumors progress, sCAFs are dynamically rewired and at

4W, a subpopulation expressing MHC class II antigen-presentation genes takes dominance. MHC class II molecules are constitutively expressed on professional antigen-presenting cells (APCs). In other cell types, including fibroblasts, the expression of MHC class II can be induced by stimuli such as interferon-γ[36,37], as shown for synovial fibroblasts in inflamed joints of rheumatoid arthritis[38]. The apCAFs recently described in pancreatic cancer[30] did not express co-stimulatory molecules. Similarly, we could not detect expression of co-stimulatory molecules in sCAFs. Whether and how activation of MHC class II in nonprofessional APCs such as sCAFs affects immune responses will be the subject of future investigation.

Metastatic CAFs are poorly defined. In our mouse model, primary tumor CAFs and metastatic CAFs clustered together into the main CAF subtypes, suggesting that both subtypes are present in the primary site and in the metastatic site. Nevertheless, primary and metastatic CAFs exhibited distinct subpopulations within each subtype, in particular within pCAFs. These changes are probably driven, to some extent, by the different environment in the lung compared to the mammary tissue. Given the observed shift between 2W and 4W primary tumor CAFs, however, our results suggest that these changes reflect the dynamic rewiring of CAFs along tumor progression, beginning at the primary site and continuing as tumors metastasize.

The coexistence of different CAF populations and their dynamic rewiring has prognostic and potentially therapeutic implications. In two independent patient cohorts, encompassing together all subtypes of breast cancer, those with higher sCAF/pCAF ratios had markedly improved survival. In the TNBC cohort, high ratios of sCAF/pCAF correlated not only with survival but also with *BRCA* mutations. *BRCA* mutations frequently lead to TNBC and the DNA damage associated with these mutations leads to increased somatic mutational load and higher T-cell infiltration[26,39]. It is plausible that the immunoregulatory activity of pCAFs inhibits T-cell activation whereas antigen-presenting sCAFs activate the immune system, leading to improved clinical outcomes. Our findings highlight the need to define and target deleterious CAF subpopulations, while enriching potentially beneficial populations, within patient cohorts with defined genetic and transcriptional landscapes.

Methods

Ethics statement. All clinical data were collected following approval by the Sheba Medical Center Institutional Review Board (IRB), protocol no. 8736-11-SMC or Ministry of Health (MOH) IRB approval for the Israel National Biobank for Research (MIDGAM), protocol no. 130-2013 or as detailed previously[40]. All animal studies were conducted in accordance with the regulations formulated by the Institutional Animal Care and Use Committee (protocol nos. 40471217-2; 09720119-1; 00470120-2).

Human patient samples. Tumor sections from five patients with ER$^+$ and six patients with TN breast cancer were obtained from MIDGAM under MOH IRB no. 130-2013 and IRB no. 8736-11-SMC and a TMA-containing cores from 72 patients with TNBC (three cores per patient), with matching H&Es and whole-tissue sections from a subset of 12 patients from this cohort, were retrieved from the archives of Sheba Medical Center under IRB no. 8736-11-SMC. All clinical data were collected following appropriate ethical approvals. For the TNBC cohort approval was given by the Sheba Medical Center IRB (protocol no. 8736-11-SMC) with full exemption for consent form for anonymized samples. For samples collected from MIDGAM, MOH IRB approval was obtained (protocol no. 130-2013). These samples were collected from patients who provided informed consent for collection, storage and distribution of samples and data for use in future research studies.

A TMA containing a subset of the molecular dataset of the METABRIC study[24] was obtained under appropriate ethical approval from the IRB for the use of biospecimens with linked pseudo-anonymized clinical data[40].

Mice. BALB/c and C57BL/6 mice were purchased from Harlan Laboratories and maintained under specific-pathogen-free conditions at the Weizmann Institute of Science (WIS) animal facility.

Cancer cell lines. The 4T1 cells expressing firefly luciferase (pLVX-Luc) were kindly provided by Z. Granot (HUJI). E0771 cells were kindly provided by R. Alon (WIS). Green fluorescent protein (GFP)-expressing 4T1 cells were generated using the FUW-GFP vector and mCherry-luc-expressing E0771 cells were generated using a luc2a-mcherry vector. The 4T1 and E0771 cells were cultured in Dulbecco's modified Eagle's medium (DMEM; Biological Industries, 01-052-1A) with 10% fetal bovine serum (FBS; Invitrogen).

Orthotopic injection to the mammary fat pad. The 8W-old BALB/c or C57BL/6 female mice were injected under anesthesia with 100,000 4T1-luc cells or 600,000 E0771 cells in ice-cold PBS, into the lower left mammary fat pad.

Normal mammary fat pad isolation and dissociation. Mammary fat pads were collected from nontumor-bearing BALB/c females (8W old for single-cell analysis, 12W old for bulk sequencing), tissue was minced and dissociated using a gentleMACS dissociator, in the presence of enzymatic digestion solution containing 1 mg ml^{-1} collagenase II (Merck Millipore, 234155), 1 mg ml^{-1} collagenase IV (Merck Millipore, C4-22) and 70 U ml^{-1} DNase (Invitrogen, 18047019) in DMEM. The samples were filtered through a 70-μm cell strainer into ice-cold MACS buffer (PBS with 0.5% BSA) and cells were pelleted by centrifugation at 350*g* for 5 min at 4 °C.

Primary tumor isolation and dissociation. At 14 or 28 d after 4T1-luc injection, animals were killed, and tumors were excised, dissociated, minced and incubated with enzymatic digestion solution containing 3 mg ml^{-1} collagenase A (Sigma Aldrich, 11088793001) and 70 U ml^{-1} DNase in RPMI 1640 (Biological Industries, 01-100-1A) for 20 min at 37 °C. To enrich for stromal cells, single-cell suspensions were incubated with anti-EpCAM (Miltenyi, 130-105-958) and anti-CD45 (Miltenyi, 130-052-301) magnetic beads, transferred to LS columns (Miltenyi, 130-042-401) and the stromal enriched (CD45, EpCAM depleted) flow-through was collected and pelleted.

Lung metastases isolation and dissociation. To allow the growth of >1 mm lung metastases, primary tumors were surgically removed under anesthesia 2W after injection of 4T1-luc cells to the mammary fat pad. The mice were imaged every 4–6 d by an in vivo imaging system to detect luciferase-positive lung metastases. At 2–3 weeks after primary tumor removal, the animals were killed, metastases-bearing lungs were excised and metastases were isolated from the lungs and dissociated in gentleMACS C tubes with an enzymatic digestion solution containing collagenase A 1.5 mg ml^{-1}, dispase II 2.5 U ml^{-1} (Sigma Aldrich, D4693) and DNase I 70 U ml^{-1} in RPMI 1640.

Flow cytometry and sorting. Staining was performed on single cells with antibodies detailed in Supplementary Table 11 for 30 min on ice. Single-stain controls were used for compensation of spectral overlap between fluorescent dyes. Propidium iodide was added shortly before samples were sorted. Cells were sorted with a BD FACSAria Fusion machine and data was analyzed using FlowJo software (Tree Star Inc.).

Single-cell index sorting. Stained cells were single-cell sorted as previously described[15]. Briefly, cells were sorted into 384-well barcoded capture plates containing 2 μl of lysis solution and barcoded poly(T) reverse-transcription primers for single-cell RNA-seq[15]. The FACS Diva v.8 'index sorting' function was activated to record marker levels of each cell and the intensities of all FACS markers were recorded and linked to each cell's position within the 384-well plate[41]. Four empty wells per 384-well plate were kept as a no-cell control for data analysis. Plates were spun down immediately after sorting, snap frozen on dry ice and stored at −80 °C until processing.

Library preparation for single-cell RNA-seq. Single-cell MARS-seq libraries were prepared as previously described[15]. In brief, messenger RNA from sorted cells was barcoded, converted into complementary DNA and pooled. Pooled samples were linearly amplified by T7 in vitro transcription and the resulting amplified RNA was fragmented and converted into a sequencing-ready library by tagging with pool barcodes and Illumina adaptor sequences during ligation, reverse transcription and PCR. Library quality and concentration were assessed as described[15].

Low-level processing and filtering. All RNA-seq libraries were sequenced using Illumina NextSeq 500 at a median sequencing depth of 28,114 reads per single cell. Sequences were mapped to the mouse genome (mm10), demultiplexed and filtered as previously described[15], extracting a set of UMIs that define distinct transcripts in single cells for further processing. We estimated the level of spurious UMIs in the data using statistics on empty MARS-seq wells median noise (2.6%). Mapping of reads was performed using HISAT v.0.1.6 (ref.[42]); reads with multiple mapping positions were excluded. Reads were associated with genes if they were mapped to an exon, using the University of California, Santa Cruz genome browser as reference. Exons of different genes that shared genomic position on the same strand were considered a single gene with a concatenated gene symbol. Cells with fewer than 1,000 UMIs were discarded from the analysis. After filtering, cells contained a median of 2,733 unique molecules per cell. All downstream analysis was performed in R (v.3.6.0).

Data processing and clustering. The MetaCell pipeline[43] was used to derive informative genes and compute cell-to-cell similarity, to compute *k*-nearest-neighbor graph covers and derive distribution of RNA in cohesive groups of cells (or metacells) and to derive strongly separated clusters using bootstrap analysis and computation of graph covers on resampled data. Default parameters were used unless otherwise stated. Clustering was performed on the $CD45^-EpCAM^-$ (Extended Data Fig. 1a) compartment of 15 samples. Cells with high expression of *Hbb-b1* or *Ptprc* were regarded as contaminants of red blood or immune cells, respectively and were discarded from subsequent analysis. Following clustering of the remaining cells (Extended Data Fig. 1d), cells with high expression of *Pecam1* and *Rgs5* were identified as endothelial cells and pericytes, respectively and discarded from further analysis. In addition, a group of 33 cells with markedly high expression of *Mki67* and *Myc* was assumed to have contamination with cancer cells and removed from further analysis.

Metacell clustering was performed over the top 10% most variable genes (high var/mean), with total expression over 50 UMIs and >2 UMIs in at least three cells, resulting in 1,017 feature genes. Resulting clusters were filtered for outliers and cells with more than fourfold deviation in expression of at least one gene were marked as outliers and discarded from further analysis. This resulted in 43 outlier cells and 8,033 cells were retained for further analysis. To annotate the resulting metacells into cell types, we used the metric $FP_{gene,mc}$, which signifies for each gene and metacell the fold change between the geometric mean of the gene within the metacell and the median geometric mean across all metacells. We used this metric to 'color' metacells for the expression of subset-specific genes such as *Gsn* and *S100a4*. Each gene was given a FP threshold and a priority index. The selected genes, priority and fold-change threshold parameters are as detailed in Supplementary Table 12.

GO enrichment analysis. Gene-set enrichment analysis was performed using Metascape (http://metascape.org).

Trajectory finding. To infer trajectories and align cells along developmental pseudo-time, we used Slingshot[19] and applied it on pCAFs of the primary tumor (2W, 4W). We chose a set of differential genes between the clusters (false discovery rate (FDR)-corrected chi-squared test, $q < 10^{-3}$, fold change >2). We performed principal-component analysis (PCA) on the log-transformed UMIs, normalized to cell size. We ran Slingshot on the top five principal components, with $Pdpn^+$ NMFs as the starting cluster.

Pareto analysis. *sCAF single-cell data.* The gene-expression dataset of NMF, 2W and 4W CAFs included 21,948 genes and 6,587 cells (3,067 sCAFs and 3,521 NMF and pCAFs). In PCA analysis of the sCAFs, cells from 2W and 4W time points formed a continuum, whereas mets formed a separate cluster. We therefore excluded mets from ParTI analysis, which focuses on continuous expression patterns. We considered cells with a total of at least 3×10^3 UMIs and genes with at least 10^3 UMIs, totaling 2,292 cells and 790 genes. Each cell was downsampled to 10^3 UMIs and each gene was log-transformed and centered by subtracting its mean.

Data dimensionality. To determine the dimensionality of the data for ParTI, we used Principal Convex Hull analysis (PCHA) to find the best-fit polytopes with $k=3$–7 vertices. We calculated the variance of the vertex positions by PCHA on bootstrapped data (resampling the cells with returns). The variance for $k=3$ and 4 is low and rises sharply for $k>4$ (Extended Data Fig. 3f), indicating that it is not possible to determine the positions of more than four vertices with high reliability. In agreement with the three-dimensionality of the tetrahedron, PCA analysis indicated that the first three principal components explain much more variance than higher order principal components (Extended Data Fig. 3e). We concluded that four vertices and the first three principal components were the appropriate choice for this analysis.

Tetrahedron significance. The variation in the vertex positions of the real data (bootstrapping) was much smaller than the variation of the vertex positions in the best-fit tetrahedron (PCHA) for 1,000 shuffled datasets ($P<0.001$; Extended Data Fig. 3g,h). We further tested the statistical significance of the tetrahedron by the *t*-ratio test as described previously[21,44]. The observed *t* ratio was significantly larger than the *t* ratios of shuffled datasets ($P=6\times10^{-3}$; Extended Data Fig. 3i).

Enrichment calculation and GO analysis. We defined enriched genes for each vertex by calculating the Spearman rank correlation between the gene's expression and the Euclidean distance of cells from the vertex. We call a gene enriched if its expression shows a correlation coefficient <-0.2 with a statistically significant *P* value controlled for multihypothesis testing by an FDR correction using the Bonferroni procedure with a threshold of 10^{-5}. GO analysis was performed using MathIOmica[45] with a cutoff of at least three genes for each GO term. To address circularity concerns stemming from using gene expression both to infer the position of the vertex and their functions, we use a leave-one-out procedure: for each enriched gene, we recompute the position of the vertices after removing the gene. We then determine which samples are closest to the new vertices and test whether the gene is still significantly enriched close to the vertex by the same method as above.

Vertex temporal ordering. We computed the relative representation of cells from each time point (2W, 4W) between the four vertices (Fig. 3d). Cells from each time point were downsampled to reach the same number (300) and the fraction of each time point in the 100 cells closest to each archetype was calculated. Error bars were calculated by bootstrapping (10^3).

Bulk RNA-seq. The 4W tumors or normal mammary fat pads from four mice each were excised, 10^4 cells were sorted from each population as described for single-cell RNA-seq, with the addition of PDPN as a positive-selection marker for pCAFs (Extended Data Fig. 1a). NMFs were taken from the $CD45^-/EpCAM^-$ population without further selection. The sCAFs were collected based on negative selection for all markers ($CD45^-EpCAM^-PDPN^-$). The cells were collected directly into lysis/binding buffer (Life Technologies) and mRNA was isolated using Dynabeads oligo (dT) (Life Technologies). RNA-seq was performed as previously described[15]. Libraries were sequenced on an Illumina NextSeq 500 machine and reads were aligned to the mouse reference genome (mm10) using STAR v.2.4.2a[46]. Duplicate reads were filtered if they aligned to the same base and had identical UMIs. Read count was performed with HTSeq-count[47] in union mode and counts were normalized using DEseq2 (ref. [48]). Representative samples from each subpopulation were used for Pearson correlation matrix (Extended Data Fig. 1h).

Tracing of host versus cancer markers in sCAFs. To test for presence of 4T1 cells in the negatively selected sCAF population we traced the LTR of a luciferase plasmid expressed in these cells. While this sequence could not be detected by single-cell RNA-seq (due to polyA selection) we could detect it by bulk RNA-seq. We therefore counted the number of reads mapped to the LTR in different populations from bulk FACS sort and normalized these to the number of reads mapped to the house keeping gene actin. The normalized LTR reads were 44-fold more abundant in bulk $EpCAM^+$ cells from the tumor (that may also contain normal epithelial mammary cells) than in sCAFs (0.011 in $EpCAM^+$ versus 0.00027 in sCAFs). We could not detect LTR reads in pCAFs and NMFs. These results suggest that the majority of sCAF do not originate from 4T1 cancer cells, however there is a low level of contamination by 4T1 cells, at least in the bulk population.

To validate these results we expressed GFP in 4T1 cells, injected these into the mammary fat pad of mice, sorted tumors by FACS to remove $PDPN^+$ and $CD45^+$ cells and further sorted for bulk RNA-seq of the following populations: (1) GFP^+EpCAM^+ (expected to include 4T1 cells); (2) GFP^+EpCAM^- (expected to include 4T1 cells that may have undergone EMT); (3) GFP^-EpCAM^+ (expected to include host epithelial cells); and (4) GFP^-EpCAM^- (expected to include sCAF, as well as a minor population of endothelial cells and pericytes). Bulk sequencing and differential gene-expression analysis confirmed that GFP^+EpCAM^+, GFP^+EpCAM^- and GFP^-EpCAM^+ populations exhibited similar patterns of gene expression, whereas GFP^-EpCAM^- cells were distinct, suggesting that $GFP^-EpCAM^-PDPN^-CD45^-$ cells do not originate from cancer cells, nor do they resemble normal epithelial cells (Supplementary Table 5). The top 20 differentially upregulated genes in GFP^-EpCAM^- cells (sCAFs) compared to GFP^+EpCAM^+ cells (4T1 cells) contain classic stromal genes such as *Cxcl12*, *Col3a1* and *Ccl4* (Supplementary Table 5). The classic epithelial marker *Krt14* is among the most differentially downregulated genes in GFP^-EpCAM^- cells compared to GFP^+EpCAM^+ cells (Supplementary Table 5).

FACS for functional assays with pCAFs. The 4W 4T1-luc primary tumors were dissociated into single-cell suspensions, incubated with red blood cell lysis buffer (BioLegend 420301) and depleted of $CD45^+$ and $EpCAM^+$ cells as described above. For pCAF enrichment, the CD45 and EpCAM depleted fraction was incubated with PDPN–biotin antibody and the PDPN-enriched cell suspension was isolated with anti-biotin magnetic beads (Miltenyi, 130-090-485). The cells were stained for Ter119-PB, CD45-BV711, EpCAM-AF488, PDPN–APC and Ly6C-PerCP/Cy5.5. $PDPN^+$ cells were gated as described in Extended Data Fig. 1a and sorted into $Ly6C^+$ and $Ly6C^-$ populations.

$CD8^+$ T-cell proliferation and activation assay. Overall, 5×10^4 $Ly6C^+$ or $Ly6C^-$ pCAFs were plated in 96 wells in RPMI 1640 supplemented with 10% FBS. Three days later, $CD8^+$ T cells were isolated from normal spleens by a positive-selection kit (CD8a (Ly-2) Microbeads, mouse, Miltenyi 130-117-044), stained with 2 μM CFSE and incubated with CD3/CD28 Dynabeads with or without $Ly6C^+$ or $Ly6C^-$ pCAFs in lymphocyte medium (RPMI 1640, 10% FBS, 1% MEM NEAA, 1% 0.5 M HEPES buffer, 1% L-glutamine, 1% sodium pyruvate and 0.0004% βM-EtOH (Biological Industries)). After 48 h, magnetic beads were removed and cells were analyzed by flow cytometry. CD25-BV711 and CD69-APC antibodies were used to determine $CD8^+$ T-cell activation levels, Ghost-Dye-Violet 450 (TONBO) was used to exclude dead cells and CFSE was used to determine $CD8^+$ T-cell proliferation. FACS analysis was performed using Kaluza software v.2.1 (Beckman Coulter).

Flow cytometry of pCAFs, sCAF and NMF markers. Tissues were collected and dissociated into single-cell suspensions as described above. For pCAF intracellular staining, cells were fixed with 4% PFA in PBS for 10 min, washed and resuspended in permeabilization/washing buffer (PBS (calcium and magnesium free), 0.1% Tween 20 (BIO BASIC) and 1% BSA) and incubated for 20 min at room temperature. For 4T1 tumors, cells were stained with CD45-BV711, EpCAM-PE/Cy7, PDPN–APC and Ly6C$^-$PerCP/Cy5.5, fixed, permeabilized and intracellularly stained with α-SMA–FITC. E0771-mCherry tumors were stained with Ghost-Dye-Violet 450 viability dye (TONBO), CD45$^-$BV711, PDPN–APC, Ly6C-PerCP/Cy5.5 and then fixed, permeabilized and intracellularly stained with α-SMA–FITC. For sCAF marker staining, live cells were stained with CD45-BV711, EpCAM-AF488, PDPN–APC and I-A/I-E-APC/Cy7.

Collagen deposition measurement in vitro. PDPN$^+$Ly6C$^+$ or Ly6C$^-$ CAFs were seeded after sorting until reaching confluency and seeded in at least three technical replicates in a concentration of 2×10^5 ml^{-1} in RPMI complete medium. The cells were left for 4 d in culture to assure confluence before preforming collagen content measurement using a commercial Sirius Red collagen staining kit (Chondrex). Images were taken with a Leica DMI8 wide-field (inverted) microscope, objective ×10/0.25, using a DFC310FX color camera.

Immunohistochemistry of mouse tissues. FFPE 4-µm sections of normal mammary fat pads, tumors or metastases were deparaffinized, treated with 1% H_2O_2 and antigen retrieval was performed with Tris-EDTA buffer (pH 9.0). Slides were blocked with 10% normal horse serum (Vector Labs, S-2000) and the antibodies listed in Supplementary Table 11 were used. Visualization was achieved with 3,30-diaminobenzidine as a chromogen (Vector Labs kit SK4100). Counterstaining was performed with Mayer hematoxylin (Sigma Aldrich MHS-16). Images were taken with a Nikon Eclipse Ci microscope.

Immunofluorescent staining of mouse and human tissues. Whole FFPE sections from mouse and human tumors and cores from the human TNBC and METABRIC TMAs, were deparaffinized and incubated in 10% neutral buffered formalin (prepared by 1:25 dilution of 37% formaldehyde solution in PBS). Antigen retrieval was performed with citrate buffer (pH 6.0) or with Tris-EDTA buffer (pH 9.0). Slides were blocked with 10% BSA + 0.05% Tween 20 and the antibodies listed in Supplementary Table 11 were diluted in 2% BSA in 0.05% PBST and used in a multiplexed manner using the OPAL kit (Akoya Biosciences), each one overnight at 4 °C. We used the following staining sequences: CK → S100A4 → PDPN → DAPI (for 4T1); S100A4 → CK → PDPN → DAPI (for E0771 and for human); S100A4 → CD45 →DAPI; or CD3 →DAPI. Whole-tumor sections from the human TNBC cohort were stained by either of the following sequences: set 1: α-SMA → S100A4 → NT5E → HLA → PDPN; set 2: α-SMA → CK → PDPN →DAPI; or set 3: S100A4 → NT5E →HLA →CK → DAPI. Each antibody was validated and optimized separately and then MxIF was optimized. Slides of mouse and whole human tumor sections were imaged with a DMi8 Leica confocal laser-scanning microscope, using HC PL APO ×20/0.75; ×40/1.3 oil-immersion; or ×60/1.4 oil-immersion objectives and HyD SP GaAsP detectors. TMA slides were imaged with an Eclipse TI-E Nikon inverted microscope, using a CFI Super Plan Fluor ×20/0.45 and DAPI/FITC/Cy3 and Cy5 cubes. Images were acquired with a cooled electron-multiplying charge-coupled device camera (IXON ULTRA 888; Andor).

Image analysis. Quantification of TMA staining was performed using the Fiji image processing platform[49]. ROIs were manually depicted to include all intact tissue areas and exclude regions of adipose tissue (due to nonspecific staining). H&Es from the TNBC TMA were used to assist in training and optimizing this step. Following background subtraction using a rolling ball with a radius of 200 pixels, the CK, S100A4 and PDPN channels were thresholded using Otsu method. The threshold of CD3 (stained and analyzed separately) was set to 2,500–65,535. All pixels above the threshold were counted as 1, and their sum was divided by the ROI (Fig. 7a). Channel/ROI scores of all replicate cores from the same patient (typically three) were averaged and the average score was used for statistical analysis. Ratios between different stains were calculated for each core and averaged for each patient. In the TNBC cohort, two patients were excluded from the analysis due to S100A4/PDPN values 3 × s.d. above average. Four patients were excluded from CD3 analysis due to unusually high background staining that could not be interpreted. All other scores collected were included in the analyses. In the METABRIC cohort, five patients were excluded from the analysis due to S100A4/PDPN values 3 × s.d. above average.

Regional analysis of cancer-adjacent and dense-stromal regions was performed as follows: we applied a threshold to the CK channel using Moments method and expanded the CK$^+$ regions using the 'Dilate' function six times. A mask generated from this image was used to define 'cancer-adjacent' regions, and the inverse mask was used to define 'dense-stromal' regions. Ratios between different stains were calculated for each region as described above. In the METABRIC cohort, owing to the small size of tumor cores, regional analysis was performed only on samples in which $0.05 <$ cancer-adjacent/total ROI < 0.95 ($n = 219$ patients).

Analysis of overlap between CAF markers in human breast tumors was performed on MxIF staining of whole-tissue FFPE sections from the TNBC cohort. Briefly, the sections were scanned by confocal microscopy as described above. In cases of staining with more than four fluorophores, we performed linear spectral unmixing. The images from each channel were then z-stacked ('Average') and a threshold was applied using Moments method to generate masks. The number of overlapping pixels between channels was quantified using the 'AND' function in the image calculator and divided by the total number of pixels of the originating channels.

Analysis of the overlap between CAF markers in murine tumors was performed on MxIF staining of whole-tissue FFPE sections. Masks for each channel were generated using Moments method. For 4T1 tumors, as CK is located only in the cytoplasm, whereas in the mouse S100A4 is observed, in some cases, also in the nucleus, we removed the nuclear region from each channel before analysis. Briefly, we applied 'Fill holes' and 'Watershed' on the DAPI mask, removed particles smaller than 8 µm^2 and created a mask from resulting particles. The 'Subtract' command was used to remove the nuclear region from each channel. The number of overlapping pixels between channels was quantified using the 'AND' function and divided by the total number of pixels of the originating channels.

Object-based analysis was performed on MxIF staining (three sets as described in the previous section) of whole-tissue FFPE sections from the TNBC cohort using QuPath[50] (v.0.2.0-m8). First, cells were segmented ('cell detection') based on nuclear staining (DAPI). Next, we trained the 'Random Trees' classifier to categorize cells as 'pCAF', 'sCAF' or 'cancer cells' (or to ignore) based on all channels in 6–7 representative images (with α-SMA, MHC and NT5E channels turned off, for blindness purposes). The classifier was applied on all images from the same set (for each set we trained a different classifier) and for each marker, the mean marker intensity per cell per image was calculated by the software. Cells with mean intensities greater than the 0.75 quantile (in each image) were defined as expressing a specific marker. After averaging for each patient the conditional probability of being positive for a marker (based on multiple images), given the cells for each cell and each marker, a test for the effect of cell and marker on that probability was conducted using ANOVA with Tukey correction for multiple comparisons. The analysis was performed separately for each of the three sets, similar trends were obtained across sets and the results of set 1 (in which all subset markers are present) are presented in Fig. 6.

Statistics and reproducibility. Clinical characteristics were compared by means of the Pearson chi-squared test for categorical variables and a Student's t-test for age (continuous variable). Recurrence-free and overall survival rates were obtained based on Kaplan–Meier estimates and a log-rank test was performed to study the difference of recurrence-free/overall survival rates. Density estimate of the divided values was obtained using integrated vase box plots and means of the two genetic groups were compared using a Student's t-test. For visualization purposes, values above two box plot whiskers were omitted from the plot, but were included in the statistical analysis (seven values from Extended Data Fig. 7e and six values from Extended Data Fig. 8c). Relative risk estimates and 95% confidence intervals were calculated utilizing Cox proportional hazard regression model for recurrence-free survival data, univariate analysis to study the effects of the variables on recurrence-free survival and multivariate analysis, considering first order interaction. Dividing continuous variables: to visualize the results of the Cox proportional hazard regression model, S100A4/PDPN and PDPN/Total ROI were divided into high and low groups by their median (in the TNBC cohort) or by a value of 1 (in the METABRIC cohort). No statistical method was used to predetermine sample size. The investigators were blinded to clinical characteristics and outcome data upon image acquisition and image analysis. All experiments were reproducible. Preliminary immunohistochemistry and MxIF staining experiments were performed on $n = 3$–5 samples and then all slides of the same cohort were stained and imaged together unless otherwise indicated.

Reporting Summary. Further information on research design is available in the Nature Research Reporting Summary linked to this article.

Data availability

Single-cell and bulk RNA-seq data that support the findings of this study have been deposited in the Gene Expression Omnibus under accession code GSE149636. All other data supporting the findings of this study are available from the corresponding author on reasonable request.

Code availability

FACS analysis was performed using FACS Diva v.8, FlowJo 10.1 and Kaluza 2.1 software. Image analysis was conducted using Fiji ImageJ 1.52g and QuPath program (v.0.2.0-m8). Read mapping of single-cell RNA-seq data was performed using HISAT v.0.1.6, followed by analysis with the custom-made MetaCell package in R (Methods). Gene-set enrichment analysis was conducted using Metascape software. Statistical analysis utilized R program (v.3.6.0; R Foundation for Statistical Computing). Packages used for analysis and visualization: tidyr v.1.0.0, reshape2 v.1.4.3, survival v.3.1-8, survminer v.0.4.6, ggplot2 v.3.2.1, ggthemes v.4.2.0, cowplot v.1.0.0 and corrplot v.0.84. Pareto data analysis was performed in Wolfram Mathematica 11.3.0, with custom-made Mathematica scripts. GO analysis was conducted with the Mathematica package MathIOmica. Scripts and auxiliary data needed to reconstruct analysis files from count matrices to full figures are available in a git repository (https://github.com/AlonLabWIS).

Received: 16 March 2020; Accepted: 19 May 2020;
Published online: 29 June 2020

References

1. McGranahan, N. et al. Clonal status of actionable driver events and the timing of mutational processes in cancer evolution. *Sci. Transl. Med.* **7**, 283ra254 (2015).
2. Pereira, B. et al. The somatic mutation profiles of 2,433 breast cancers refines their genomic and transcriptomic landscapes. *Nat. Commun.* **7**, 11479 (2016).
3. Tabassum, D. P. & Polyak, K. Tumorigenesis: it takes a village. *Nat. Rev. Cancer* **15**, 473–483 (2015).
4. Hanahan, D. & Coussens, L. M. Accessories to the crime: functions of cells recruited to the tumor microenvironment. *Cancer Cell.* **21**, 309–322 (2012).
5. Kalluri, R. & Zeisberg, M. Fibroblasts in cancer. *Nat. Rev. Cancer* **6**, 392–401 (2006).
6. Gascard, P. & Tlsty, T. D. Carcinoma-associated fibroblasts: orchestrating the composition of malignancy. *Genes Dev.* **30**, 1002–1019 (2016).
7. Pallangyo, C. K., Ziegler, P. K. & Greten, F. R. IKKβ acts as a tumor suppressor in cancer-associated fibroblasts during intestinal tumorigenesis. *J. Exp. Med.* **212**, 2253–2266 (2015).
8. Su, S. et al. CD10($^{+}$)GPR77($^{+}$) cancer-associated fibroblasts promote cancer formation and chemoresistance by sustaining cancer stemness. *Cell.* **172**, 841–856 (2018).
9. Costa, A. et al. Fibroblast heterogeneity and immunosuppressive environment in human breast cancer. *Cancer Cell.* **33**, 463–479 e410 (2018).
10. Raz, Y. et al. Bone marrow-derived fibroblasts are a functionally distinct stromal cell population in breast cancer. *J. Exp. Med.* **215**, 3075–3093 (2018).
11. Cirri, P. & Chiarugi, P. Cancer-associated fibroblasts: the dark side of the coin. *Am. J. Cancer Res.* **1**, 482–497 (2011).
12. Bochet, L. et al. Adipocyte-derived fibroblasts promote tumor progression and contribute to the desmoplastic reaction in breast cancer. *Cancer Res.* **73**, 5657–5668 (2013).
13. Sugimoto, H., Mundel, T. M., Kieran, M. W. & Kalluri, R. Identification of fibroblast heterogeneity in the tumor microenvironment. *Cancer Biol Ther.* **5**, 1640–1646 (2006).
14. Bartoschek, M. et al. Spatially and functionally distinct subclasses of breast cancer-associated fibroblasts revealed by single cell RNA sequencing. *Nat. Commun.* **9**, 5150 (2018).
15. Jaitin, D. A. et al. Massively parallel single-cell RNA-seq for marker-free decomposition of tissues into cell types. *Science* **343**, 776–779 (2014).
16. Baran, Y. et al. MetaCell: analysis of single-cell RNA-seq data using *k*-nn graph partitions. *Genome Biol.* **20**, 206 (2019).
17. Yates, L. R. et al. Subclonal diversification of primary breast cancer revealed by multiregion sequencing. *Nat. Med.* **21**, 751–759 (2015).
18. Murtaza, M. et al. Multifocal clonal evolution characterized using circulating tumour DNA in a case of metastatic breast cancer. *Nat. Commun.* **6**, 8760 (2015).
19. Street, K. et al. Slingshot: cell lineage and pseudotime inference for single-cell transcriptomics. *BMC Genomics.* **19**, 477 (2018).
20. Karnoub, A. E. et al. Mesenchymal stem cells within tumour stroma promote breast cancer metastasis. *Nature* **449**, 557–563 (2007).
21. Hart, Y. et al. Inferring biological tasks using Pareto analysis of high-dimensional data. *Nat. Methods* **12**, 233–235 (2015). 233 p following 235.
22. Korem, Y. et al. Geometry of the gene expression space of individual cells. *PLoS Comput. Biol.* **11**, e1004224 (2015).
23. Adler, M., Mayo, A., Korem Kohanim, Y. & Tendler, A. Continuum of gene-expression profiles provides spatial division of labor within a differentiated cell type. *Cell Syst.* **8**, 43–52 (2019).
24. Rueda, O. M. et al. Dynamics of breast-cancer relapse reveal late-recurring ER-positive genomic subgroups. *Nature* **567**, 399–404 (2019).
25. Peshkin, B. N., Alabek, M. L. & Isaacs, C. BRCA1/2 mutations and triple negative breast cancers. *Breast Dis.* **32**, 25–33 (2010).
26. Nolan, E. et al. Combined immune checkpoint blockade as a therapeutic strategy for BRCA1-mutated breast cancer. *Sci. Transl. Med.* **9**, eaal4922 (2017).
27. Almendro, V. et al. Inference of tumor evolution during chemotherapy by computational modeling and in situ analysis of genetic and phenotypic cellular diversity. *Cell Rep.* **6**, 514–527 (2014).
28. Lambert, G. et al. An analogy between the evolution of drug resistance in bacterial communities and malignant tissues. *Nat. Rev. Cancer* **11**, 375–382 (2011).
29. Costa-Silva, B. et al. Pancreatic cancer exosomes initiate pre-metastatic niche formation in the liver. *Nat. Cell Biol.* **17**, 816–826 (2015).
30. Elyada, E. et al. Cross-species single-cell analysis of pancreatic ductal adenocarcinoma reveals antigen-presenting cancer-associated fibroblasts. *Cancer Discov.* **9**, 1102–1123 (2019).
31. Li, H. et al. Dysfunctional CD8 T cells form a proliferative, dynamically regulated compartment within human melanoma. *Cell.* **176**, 775–789 (2019).
32. Ohlund, D. et al. Distinct populations of inflammatory fibroblasts and myofibroblasts in pancreatic cancer. *J. Exp. Med.* **214**, 579–596 (2017).
33. Tirosh, I. et al. Dissecting the multicellular ecosystem of metastatic melanoma by single-cell RNA-seq. *Science* **352**, 189–196 (2016).
34. Ohlund, D., Elyada, E. & Tuveson, D. Fibroblast heterogeneity in the cancer wound. *J. Exp. Med.* **211**, 1503–1523 (2014).
35. Quante, M. et al. Bone marrow-derived myofibroblasts contribute to the mesenchymal stem cell niche and promote tumor growth. *Cancer Cell.* **19**, 257–272 (2011).
36. Ilangumaran, S. et al. A positive regulatory role for suppressor of cytokine signaling 1 in IFN-λ-induced MHC class II expression in fibroblasts. *J. Immunol.* **169**, 5010–5020 (2002).
37. Waldburger, J. M., Suter, T., Fontana, A., Acha-Orbea, H. & Reith, W. Selective abrogation of major histocompatibility complex class II expression on extrahematopoietic cells in mice lacking promoter IV of the class II transactivator gene. *J. Exp. Med.* **194**, 393–406 (2001).
38. Boots, A. M., Wimmers-Bertens, A. J. & Rijnders, A. W. Antigen-presenting capacity of rheumatoid synovial fibroblasts. *Immunology* **82**, 268–274 (1994).
39. Lord, C. J. & Ashworth, A. BRCAness revisited. *Nat. Rev. Cancer* **16**, 110–120 (2016).
40. Curtis, C. et al. The genomic and transcriptomic architecture of 2,000 breast tumours reveals novel subgroups. *Nature* **486**, 346–352 (2012).
41. Paul, F. et al. Transcriptional heterogeneity and lineage commitment in myeloid progenitors. *Cell.* **163**, 1663–1677 (2015).
42. Kim, D., Langmead, B. & Salzberg, S. L. HISAT: a fast spliced aligner with low memory requirements. *Nat. Methods* **12**, 357–360 (2015).
43. Giladi, A. et al. Single-cell characterization of haematopoietic progenitors and their trajectories in homeostasis and perturbed haematopoiesis. *Nat. Cell Biol.* **20**, 836–846 (2018).
44. Shoval, O. et al. Response to comment on "evolutionary trade-offs, Pareto optimality, and the geometry of phenotype space". *Science.* **339**, 757 (2013).
45. Mias, G. I. et al. MathIOmica: an integrative platform for dynamic omics. *Sci. Rep.* **6**, 37237 (2016).
46. Dobin, A. et al. STAR: ultrafast universal RNA-seq aligner. *Bioinformatics* **29**, 15–21 (2013).
47. Anders, S., Pyl, P. T. & Huber, W. HTSeq–a Python framework to work with high-throughput sequencing data. *Bioinformatics.* **31**, 166–169 (2015).
48. Love, M. I., Huber, W. & Anders, S. Moderated estimation of fold change and dispersion for RNA-seq data with DESeq2. *Genome Biol.* **15**, 550 (2014).
49. Schindelin, J. et al. Fiji: an open-source platform for biological-image analysis. *Nat. Methods* **9**, 676–682 (2012).
50. Bankhead, P. et al. QuPath: open source software for digital pathology image analysis. *Sci. Rep.* **7**, 16878 (2017).

Acknowledgements

We thank O. Golani and Y. Addadi (MICC Cell Observatory, WIS) for their assistance with imaging and image analysis. We thank V. Kiss (Department of Biomolecular Sciences, WIS) for his assistance with imaging. We thank Z. Granot (HUJI) and R. Alon for providing cell lines. We thank members of the Scherz-Shouval laboratory for valuable input on the manuscript. U.A. is supported by Cancer Research UK (grant C19767/A27145). I.A. is an Eden and Steven Romick Professorial Chair, supported by Merck KGaA, Darmstadt, Germany, the Chan Zuckerberg Initiative, the HHMI International Scholar award, the European Research Council Consolidator Grant (ERC-COG) 724471- HemTree2.0, an SCA award of the Wolfson Foundation and Family Charitable Trust, the Thompson Family Foundation, an MRA Established Investigator Award (509044), the Israel Science Foundation (703/15), the Ernest and Bonnie Beutler Research Program for Excellence in Genomic Medicine, the Helen and Martin Kimmel award for innovative investigation, the NeuroMac DFG/Transregional Collaborative Research Center Grant, an International Progressive MS Alliance/NMSS PA-1604 08459 and an Adelis Foundation grant. R.S.S. is supported by the Israel Science Foundation (grant nos. 401/17 and 1384/1), the European Research Council (ERC grant agreement 754320), the Israel Cancer Research Fund, the Laura Gurwin Flug Family Fund, the Peter and Patricia Gruber Awards, the Comisaroff Family Trust, the Estate of Annice Anzelewitz and the Estate of Mordecai M. Roshwal. R.S.S. is the incumbent of the Ernst and Kaethe Ascher Career Development Chair in Life Sciences.

Author contributions

G.F. designed, performed and analyzed experiments and wrote the manuscript. O.L.-G., C.B., C.H., M.P.-F., H.L. and S.M. designed and performed the experiments. E.D, A.G.

and A.M. designed and performed bioinformatic analysis. Y.S. designed and performed statistical and image analysis. R.N. assisted with image acquisition and designed image analysis. M.D., N.B.-L., I.B, H.R.A., C.C. and E.N.-G.-Y. provided clinical samples and intellectual input. C.C., M.D. and E.N.-G.-Y. edited the manuscript. U.A. directed and designed computational analysis and wrote the manuscript. I.A. directed, designed and analyzed experiments and wrote the manuscript. R.S.S. directed, designed and analyzed experiments and wrote the manuscript.

Competing interests

The authors declare no competing interests.

Additional information

Extended data is available for this paper at https://doi.org/10.1038/s43018-020-0082-y.

Supplementary information is available for this paper at https://doi.org/10.1038/s43018-020-0082-y.

Correspondence and requests for materials should be addressed to I.A. or R.S.-S.

Reprints and permissions information is available at www.nature.com/reprints.

Publisher's note Springer Nature remains neutral with regard to jurisdictional claims in published maps and institutional affiliations.

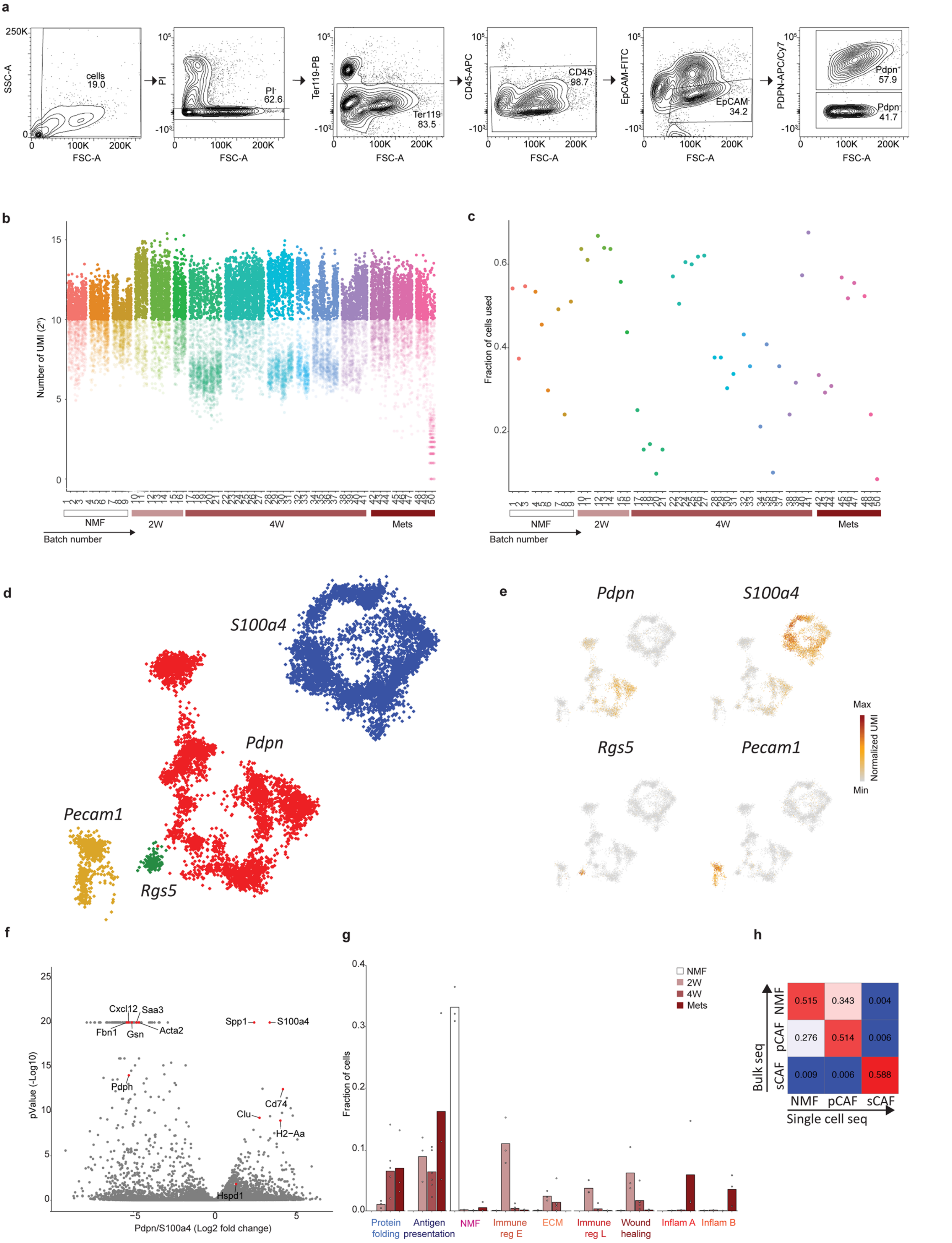

Extended Data Fig. 1 | See next page for caption.

Extended Data Fig. 1 | A single cell map of breast cancer stroma. a, Sorting strategy**:** All live single cells (PI negative cells after debris and doublet exclusion) staining negative for Ter119 (Red blood cells); CD45 (immune); and EpCAM (epithelial) were collected and single cell sorted. PDPN was used for index sorting of pCAFs. Data are combined from 8 independent experiments, with a total n = 15 mice. FACS plots from a representative 4 W tumor are shown. **b-c**, Quality control metrics of single cells analyzed in this study. **b**, Total unique molecular identifier (UMI) per cell. Cells are grouped by batch (plate) and color-coded by biological replicate (mouse). The time point for each batch is indicated. Cells with less than 1,000 UMI were discarded from the analysis. **c**, Fraction of analyzed cells/batch after filtering. Batches are grouped and color-coded as described in **b**. **d**, Single cell RNA-seq data from n = 8987 QC positive cells staining negative for Ter119, CD45 and EpCAM was analyzed and clustered using the MetaCell algorithm, resulting in a two-dimensional projection of cells from 15 mice. 88 meta-cells were associated with 4 broad clusters, annotated and marked by color code. **e**, Expression of the hallmark genes for the 4 clusters presented in **d** on top of the two-dimensional projection of breast cancer stroma. Colors indicate log transformed UMI counts normalized to total counts per cell. **f**, Volcano plot displaying differentially expressed genes between *Pdpn*$^+$ fibroblasts and *S100a4*$^+$ fibroblasts (see also supplementary table 4). Marker genes for NMF, pCAF, and sCAF are highlighted. A total of n = 8033 cells was analyzed using FDR adjusted two-sided chi square test. **g**, Fraction of cells originated from each mouse and subset, from all cells originated in their time point. Bar values represent the mean fraction values. Time points and subclasses are annotated and colored as in Fig. 1d. **h**, Squared Pearson correlation matrix for n = 1045 genes between bulk and single-cell RNA-sequencing results for NMF, pCAF, and sCAF.

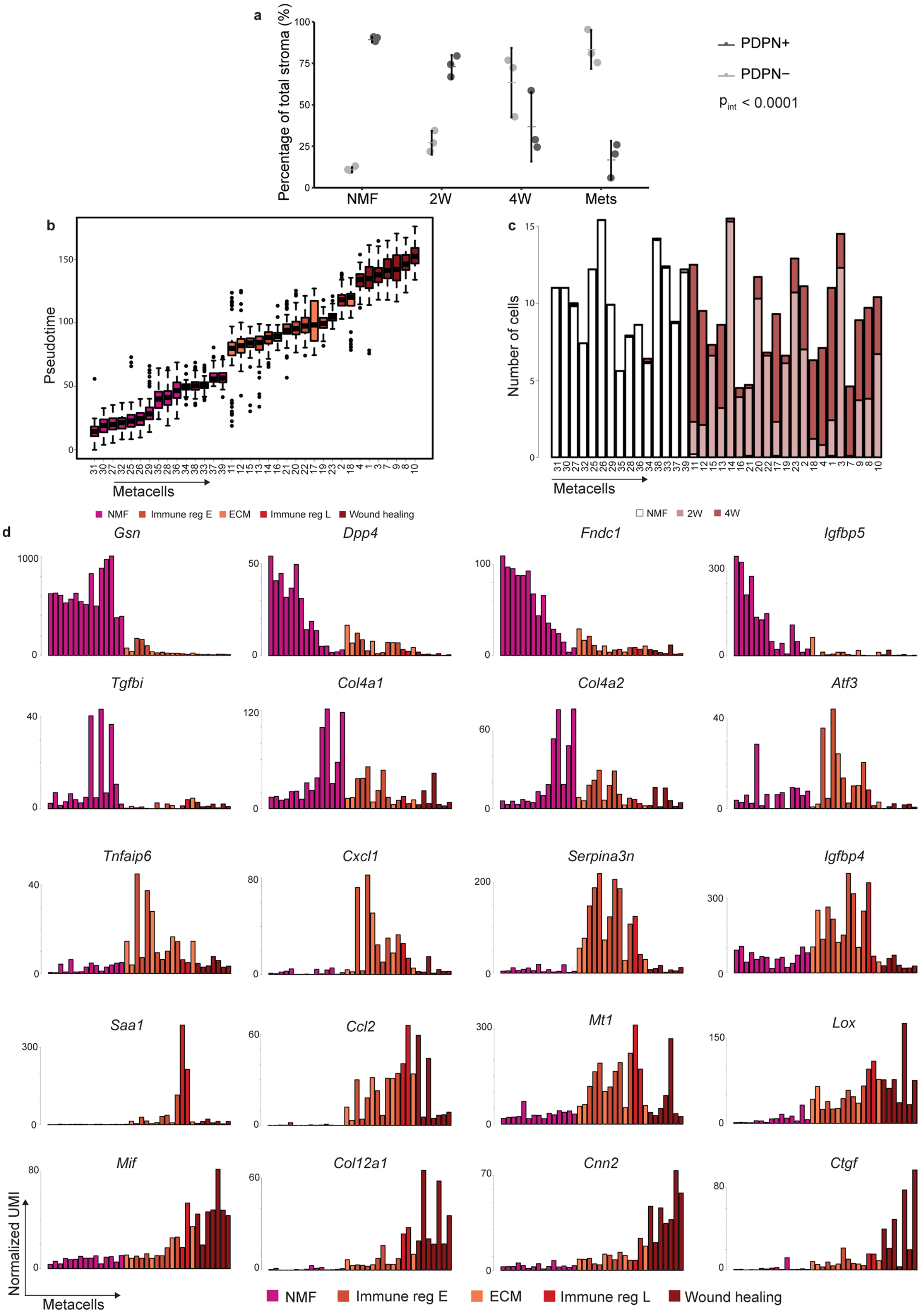

Extended Data Fig. 2 | See next page for caption.

Extended Data Fig. 2 | *Pdpn*+ fibroblasts undergo dynamic changes in gene expression and subset composition during tumor progression. a, Cell-surface PDPN protein expression levels obtained from the sorting data were used to quantify the percent of PDPN$^+$ and PDPN$^-$ cells in the CD45$^-$EpCAM$^-$ stroma in the different time points. Data are combined from 7 independent experiments; n = 3 mice per group. Error bars represent 95% CI of the mean. P-value of the two-way ANOVA interaction between fibroblast subtype and time point is presented. **b**, Pseudo-time of expression for individual metacells (color coded by functional subclasses as in Fig. 2) included in the slingshot analysis. A total of n = 3465 cells was analyzed. Box plots display median bar, first–third quartile box and 5th–95th percentile whiskers. **c**, Distribution of cells across time points (color coded) within metacells included in the slingshot analysis. Metacell numbers and order are consistent across all figure panels and match the order in Fig. 2. **d**, Expression of hallmark NMF and pCAF genes (additional to those presented in Fig. 2e) across metacells (average UMI/cell), ordered by pseudo-time.

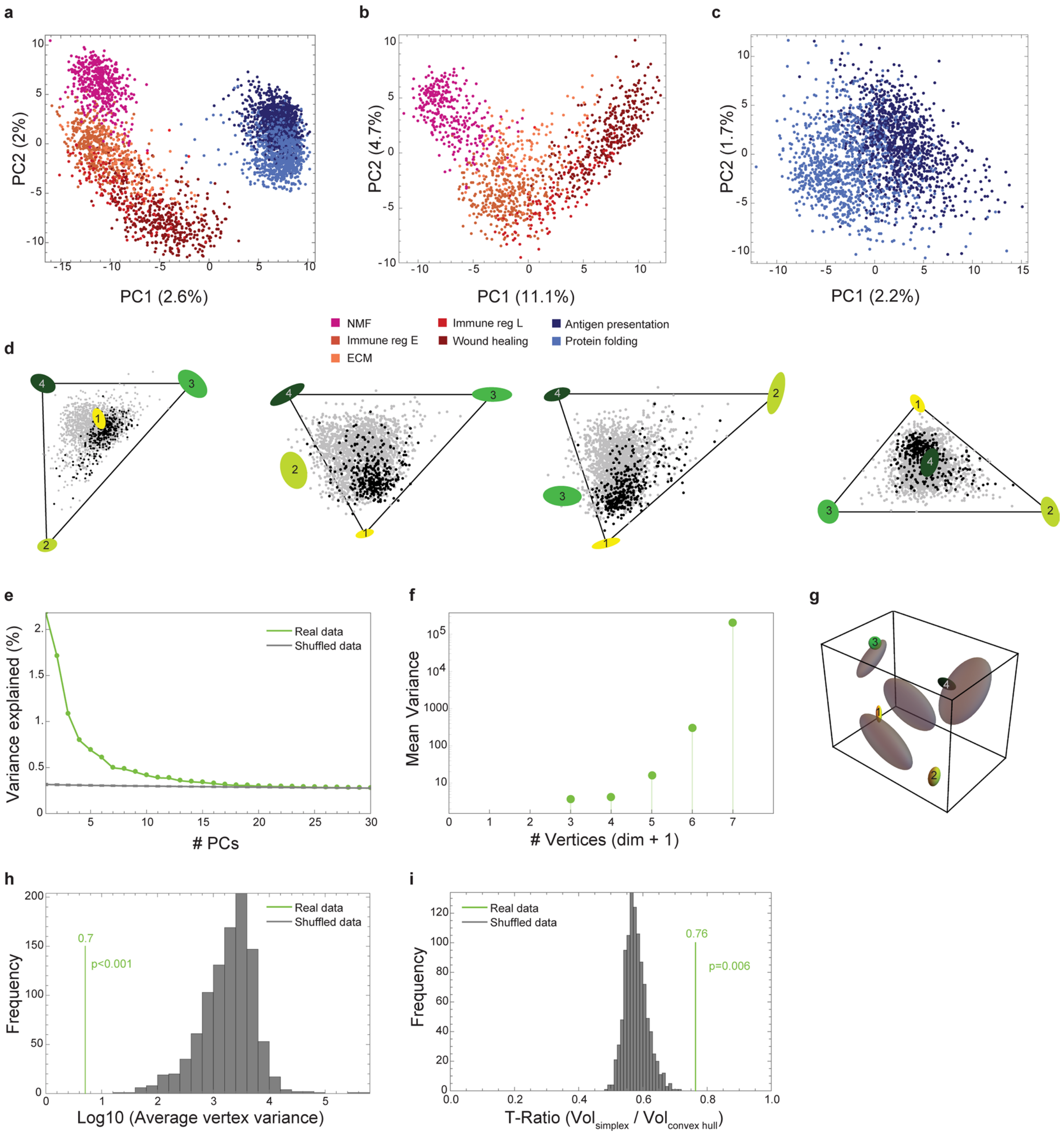

Extended Data Fig. 3 | pCAFs and NMFs form a curve in gene-expression space, whereas a tetrahedron describes sCAF gene expression. a, PCA analysis of NMF, and pCAF and sCAF from 2W and 4W, color coded according to the subclasses defined in Fig. 1c. n = 3703 cells. **b-c**, PCA analyses for NMF and pCAF (**b**) and for sCAF (**c**) color coded as in **a**. n = 3703 cells. **d**, Data projected on the four faces of the tetrahedron. **e**, Explained variance as a function of the number of PCs (real data) vs. shuffled. Note that the total variance explained by the first 3 PCs, about 5%, is typical of single-cell gene expression data[22]. **f**, Variance of vertex positions as a function of the number of vertices considered, using PCHA with k=3-7 vertices. **g**, Variation of vertex position (bootstrapping) for the real data (ellipses color-coded as in Fig. 3) *vs* shuffled data (grey ellipses). **h**, Histogram depicting the average variation of vertex positions calculated for the real data (green) *vs* multiple runs of shuffled data (grey). **i**, Histogram depicting the ratio between the volumes of the convex hull of the data and the minimal enclosing tetrahedron (t-ratio). The t-ratio of the real data (green) is compared to t-ratios of shuffled data (1000 shuffles; grey).

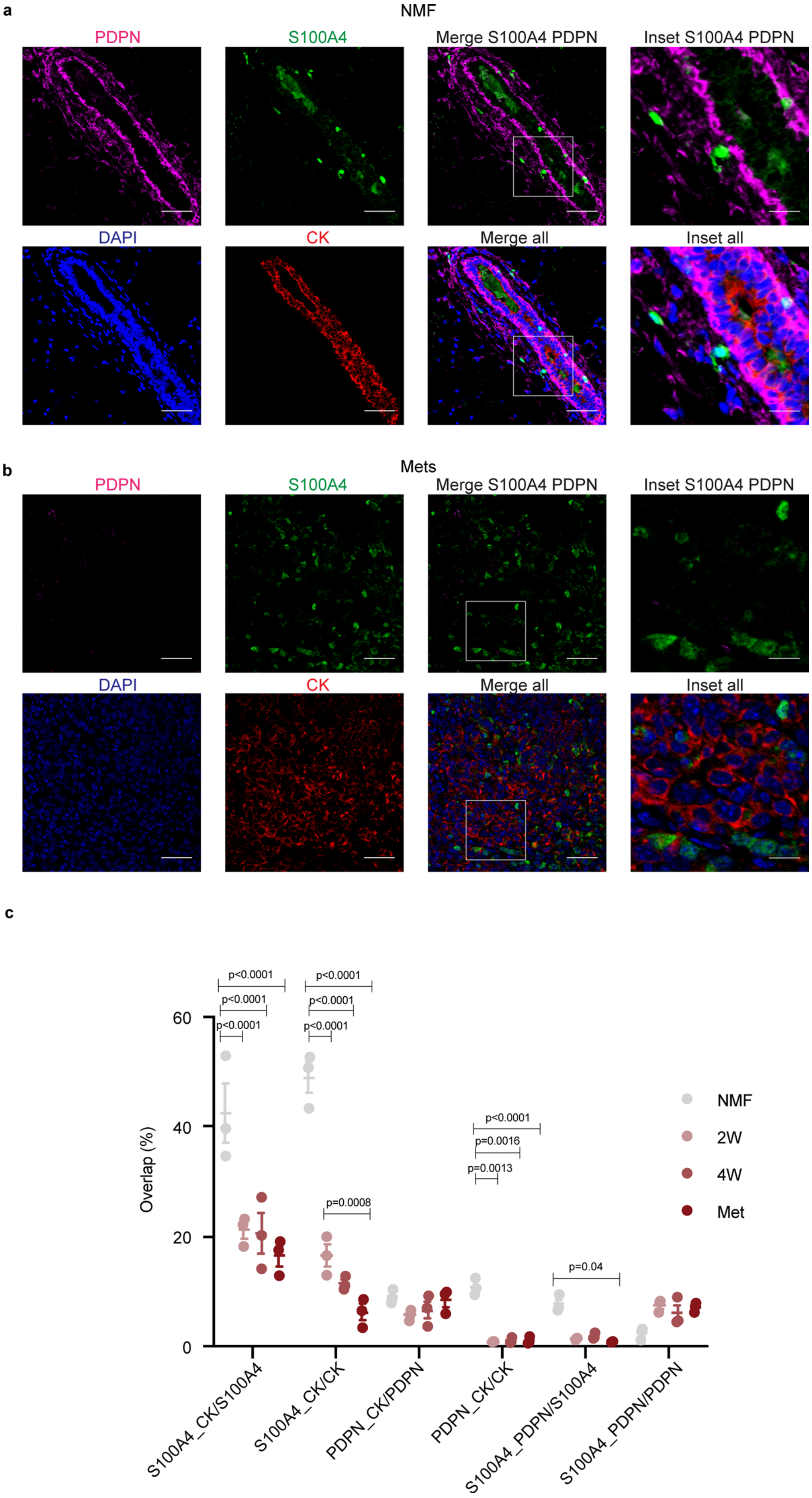

Extended Data Fig. 4 | See next page for caption.

Extended Data Fig. 4 | PDPN and S100A4 proteins mark distinct types of cells in 4T1 mouse tumors, the majority of which are CK-negative. a, **b**, Representative images of normal mammary fat pads (NMF; **a**) and lung metastases (Mets; **b**) (see Fig. 4a) stained with antibodies against the indicated proteins. n = 3 mice per time point; Scale bar = 50µm, inset scale bar = 17µm. **c**, Quantification of the average overlap between CK, PDPN, and S100A4 staining in NMFs, primary tumors (2W and 4W) and Mets. Points represent the number of overlapping pixels between two channels, divided by the total number of pixels of the originating channels, in n = 3 biological replicates (each dot is an average of 9 images per mouse). Mean ± SEM, p-values were calculated by two-way ANOVA followed by Tukey's multiple comparisons test.

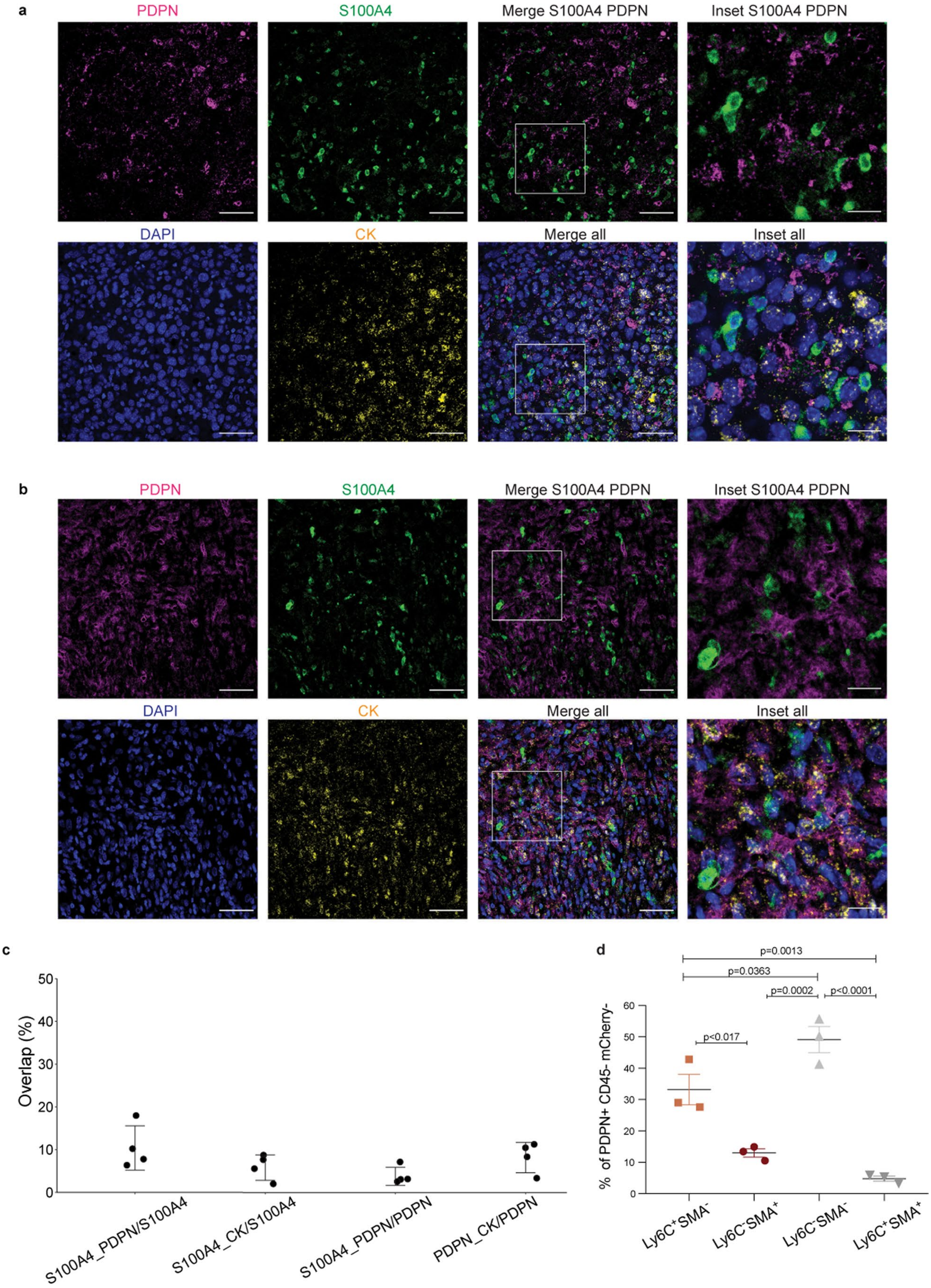

Extended Data Fig. 5 | See next page for caption.

Extended Data Fig. 5 | PDPN and S100A4 proteins mark distinct types of cells in E0771 mouse tumors, the majority of which are CK-negative. a, **b**, E0771 cancer cells were injected into the mammary fad pad of C57BL/6 mice. 4W post injection the tumors were excised and fixed. Formalin fixed paraffin embedded (FFPE) tissue sections were immunostained with antibodies against the indicated proteins (n = 4 mice in two independent experiments). Representative images from 2 different mice are shown in (**a)** and (**b)**. Scale bar = 50 µm, inset scale bar = 17µm. **c**, Quantification of the average overlap between CK, PDPN, and S100A4 staining in E0771 tumors. n = 4 mice in two independent experiments, 3-7 images per mouse. Mean ±SD, P-values were calculated by two-way ANOVA correcting for multiple comparisons and were not found to be significant ($p > 0.05$), no multiple comparison test was performed. **d**, FACS analysis of Ly6C and α-SMA expression in CD45$^-$mCherry$^-$PDPN$^+$ cells freshly harvested from 4W E0771 tumors and immediately fixed. The results from n = 3 biological replicates are quantified and analyzed utilizing one-way ANOVA followed by Tukey's multiple comparisons test, Mean ±SEM.

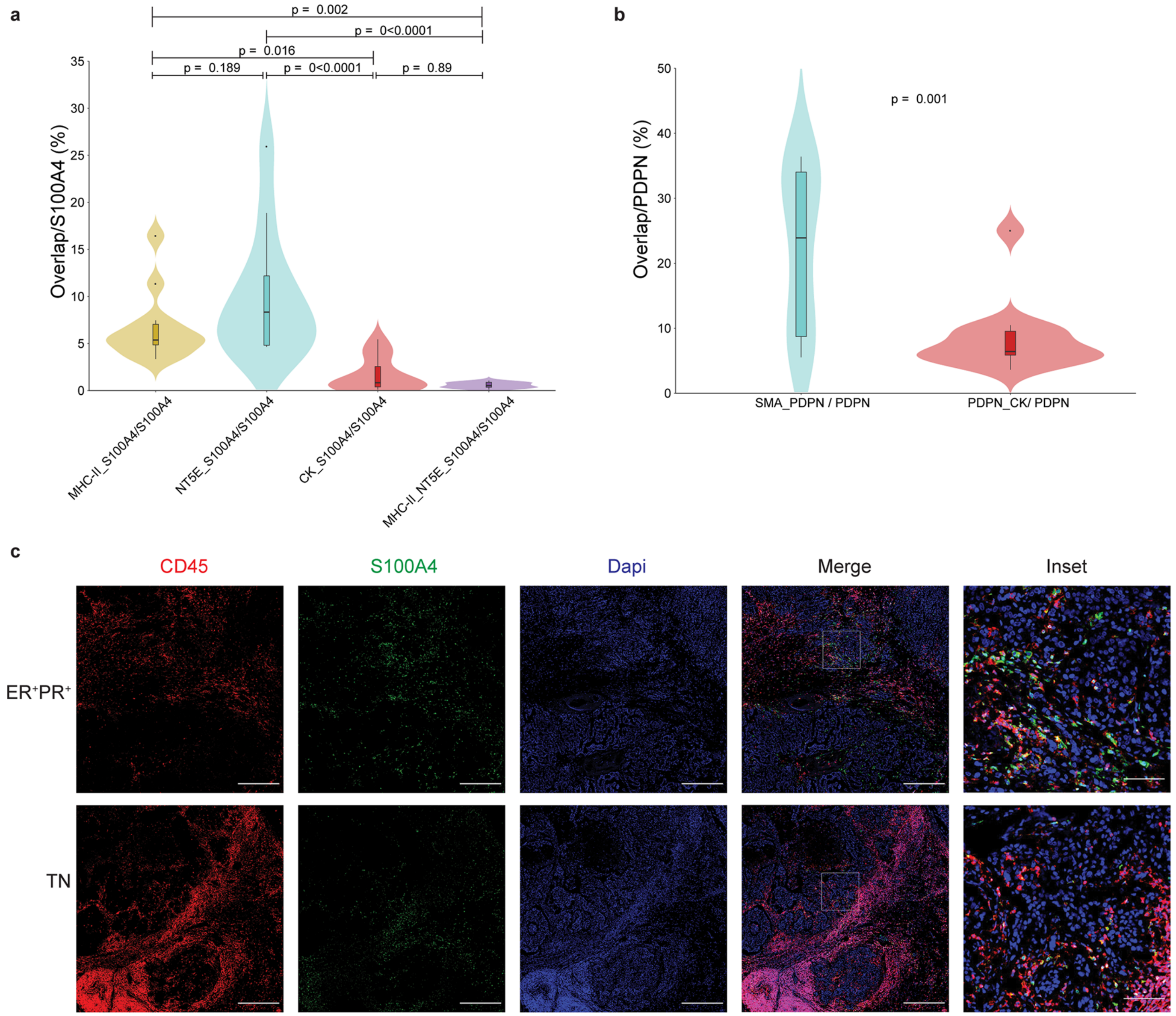

Extended Data Fig. 6 | Subsets of human sCAFs express MHC class II and NT5E, whereas a subset of pCAFs expresses α-SMA. a, **b**, The overlap between S100A4, CK, MHC-II and NT5E stains (**a**; n = 12 patients, average scores of 3 images per patient) and between PDPN, CK, and α-SMA stains (**b**; n = 14 patients, average scores of 2-4 images per patient) in TNBC patients. Median is presented with 1st and 3rd quartiles, with untrimmed violin plot overlay. P-values were calculated by two-way ANOVA followed by Tuckey's multiple comparisons test. **c**, Representative images of MxIF staining of serial sections from the same patients presented in Fig. 6a with antibodies against the indicated proteins. Scale bar = 500 µm.; inset scale bar = 90 µm.

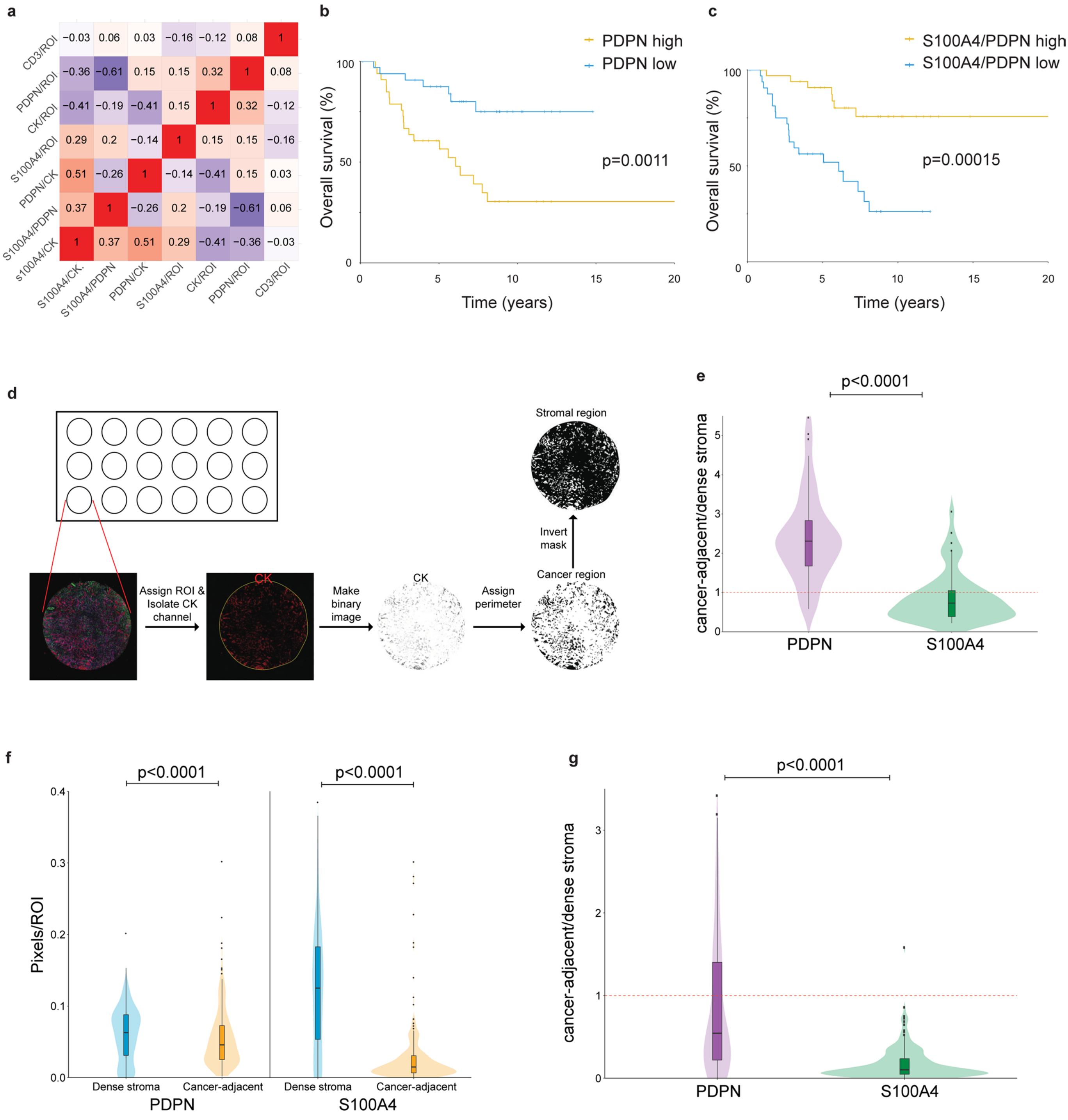

Extended Data Fig. 7 | pCAFs tend to localize to cancer-adjacent regions more often than sCAFs in human breast cancer patients. a, Heat map showing Pearson's correlation coefficients of the staining scores for different cell type markers (n = 70 patients). **b**, **c**, The association with overall survival of PDPN (**b**) or S100A4/PDPN (**c**) scored and classified as in Fig. 7b was assessed by KM analysis (n = 70 patients, P-values were calculated using log-rank test, two-sided). **d**, Illustration of the regional analysis workflow. **e**, The ratio of cancer-adjacent/dense stroma PDPN and S100A4 staining was determined for each core in the TNBC TMA (See also Fig. 7d). n = 70, median is presented with 1st and 3rd quartiles with trimmed violin plot overlay, P-value was calculated using two-sided Wilcoxon matched pairs signed-rank test. **f**, **g**, Cancer-adjacent regions and regions of dense stroma were determined for each core in the METABRIC TMA based on CK staining (see Methods section), PDPN and S100A4 staining in each region was scored (**f**) and the ratio of cancer-adjacent/dense stroma PDPN and S100A4 staining was determined (**g**). n = 219, median is presented with 1st and 3rd quartiles with trimmed violin plot overlay, P-value was calculated using two-sided Wilcoxon matched pairs signed rank test.

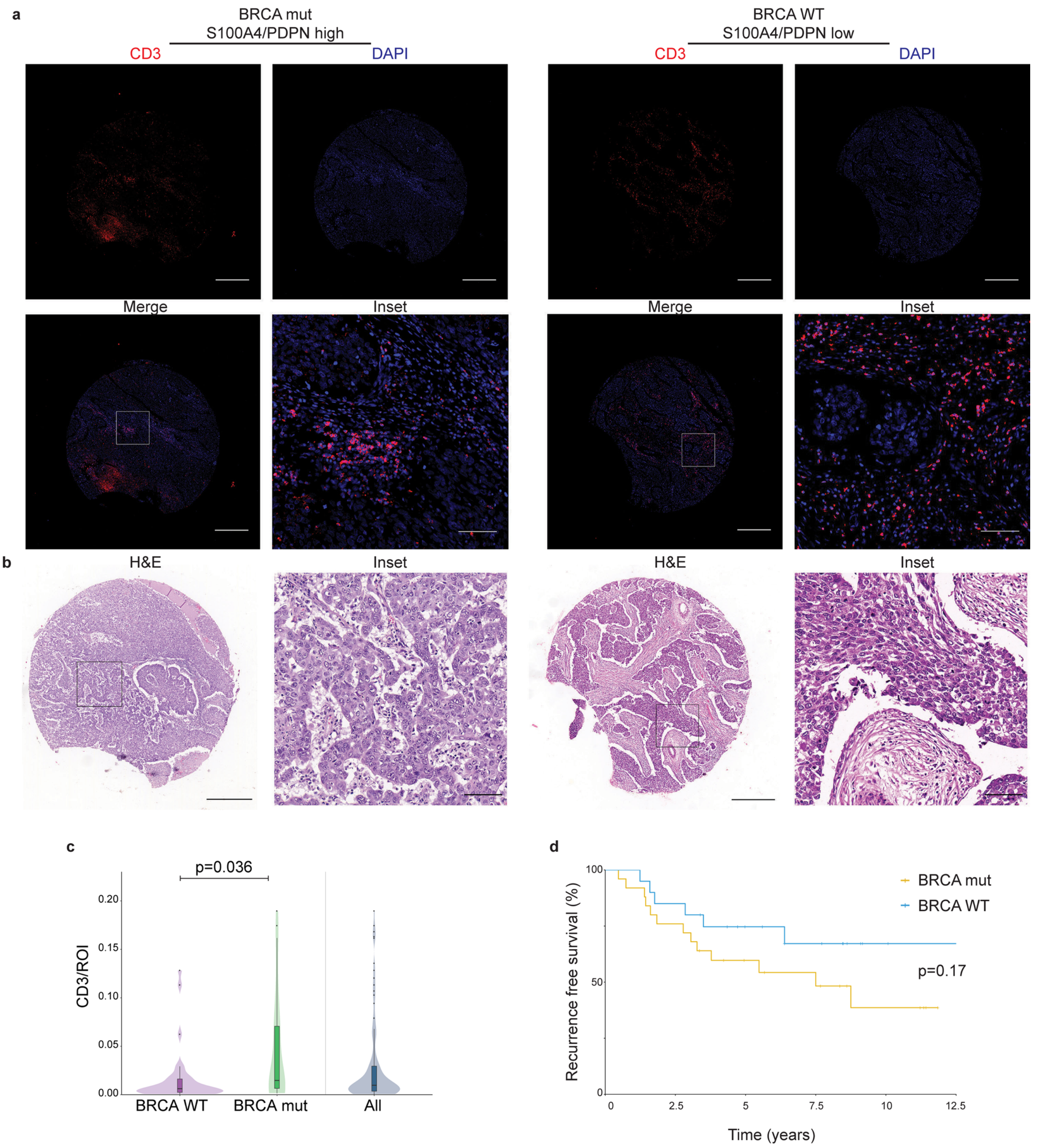

Extended Data Fig. 8 | *BRCA* status is not significantly correlated with recurrence free survival in a cohort of TNBC patients. a, CD3 and DAPI staining was performed on n = 68 patients from the TNBC cohort. Representative staining in a *BRCA* mutated (mut) patient and a *BRCA* WT patient is shown. **b**, Representative H&E stains of a *BRCA* mutated (mut) patient and a *BRCA* WT patient are shown (n = 25 *BRCA* WT; n = 20 *BRCA* mut; Serial sections of the same cores used in Fig. 8a are shown in **a** and **b**). Scale bar = 500µm; inset scale bar = 80µm. **c**, Box plot depicting CD3 staining scores (see Methods section) in patients with known *BRCA* status from our TNBC cohort (n = 23 *BRCA* WT; n = 20 *BRCA* mut) as well as the total TNBC cohort (All, n = 68). Median is presented with 1st and 3rd quartiles with trimmed violin plot overlay. P-value was calculated using a two-sided Student's t-test. **d**, TNBC patients were stratified by *BRCA* mutational status and the association with recurrence free survival was assessed by KM analysis. n = 45, P-value was calculated using two-sided log rank test.

nature research

Corresponding author(s): Ruth Scherz-Shouval

Last updated by author(s): Apr 30, 2020

Reporting Summary

Nature Research wishes to improve the reproducibility of the work that we publish. This form provides structure for consistency and transparency in reporting. For further information on Nature Research policies, see Authors & Referees and the Editorial Policy Checklist.

Statistics

For all statistical analyses, confirm that the following items are present in the figure legend, table legend, main text, or Methods section.

n/a	Confirmed	
□	☒	The exact sample size (*n*) for each experimental group/condition, given as a discrete number and unit of measurement
□	☒	A statement on whether measurements were taken from distinct samples or whether the same sample was measured repeatedly
□	☒	The statistical test(s) used AND whether they are one- or two-sided *Only common tests should be described solely by name; describe more complex techniques in the Methods section.*
□	☒	A description of all covariates tested
□	☒	A description of any assumptions or corrections, such as tests of normality and adjustment for multiple comparisons
□	☒	A full description of the statistical parameters including central tendency (e.g. means) or other basic estimates (e.g. regression coefficient) AND variation (e.g. standard deviation) or associated estimates of uncertainty (e.g. confidence intervals)
□	☒	For null hypothesis testing, the test statistic (e.g. *F*, *t*, *r*) with confidence intervals, effect sizes, degrees of freedom and *P* value noted *Give P values as exact values whenever suitable.*
☒	□	For Bayesian analysis, information on the choice of priors and Markov chain Monte Carlo settings
☒	□	For hierarchical and complex designs, identification of the appropriate level for tests and full reporting of outcomes
□	☒	Estimates of effect sizes (e.g. Cohen's *d*, Pearson's *r*), indicating how they were calculated

Our web collection on statistics for biologists contains articles on many of the points above.

Software and code

Policy information about availability of computer code

Data collection

FACS data was collected with FACSDiva v8 software.
Microscopy data was collected using Leica Application Suite x 3.5.2 and nis-elements 4.40 softwares.

Data analysis

FACS analysis was done using FACSDiva v8, FlowJo 10.1 and Kaluza 2.1 softwares.
Image analysis was done using Fiji ImageJ 1.52g and QuPath program (Version 0.2.0-m8).
Read mapping of Single cell RNA-seq data was performed using HISAT version 0.1.6, followed by analysis with the custom made MetaCell package in R, see Methods for details.
Gene set enrichment analysis was done using Metascape software.
Statistical analysis utilized R program (version 3.6.0).
Pareto data analysis was done in Wolfram Mathematica 11.3.0, with custom made Mathematica scripts. GO analysis was done with the Mathematica package MathIOmica. Scripts and auxiliary data needed to reconstruct analysis files from count matrices to full figures are available in a git repository (https://github.com/AlonLabWIS).

For manuscripts utilizing custom algorithms or software that are central to the research but not yet described in published literature, software must be made available to editors/reviewers. We strongly encourage code deposition in a community repository (e.g. GitHub). See the Nature Research guidelines for submitting code & software for further information.

Data

Policy information about availability of data

All manuscripts must include a data availability statement. This statement should provide the following information, where applicable:

- Accession codes, unique identifiers, or web links for publicly available datasets
- A list of figures that have associated raw data
- A description of any restrictions on data availability

All RNA-seq data from this study was deposited in the in the Gene Expression Omnibus (GEO) number GSE149636. Figures 1 and S1 are supported by this data.

Human MxIF data is available upon request. Code used for image analysis with Fiji software will be available upon request.

Field-specific reporting

Please select the one below that is the best fit for your research. If you are not sure, read the appropriate sections before making your selection.

☒ Life sciences ☐ Behavioural & social sciences ☐ Ecological, evolutionary & environmental sciences

For a reference copy of the document with all sections, see nature.com/documents/nr-reporting-summary-flat.pdf

Life sciences study design

All studies must disclose on these points even when the disclosure is negative.

Sample size	For scRNA-seq we sequenced and analyzed 9094 stromal cells from 15 female mice as detailed in Methods. This allows an extensive coverage of all distinct transcriptional profiles and complies with technical standards in the field. Full description of sample sizes is detailed in Supplementary table 1. Sample size was determined based on previous studies. For human MxIF staining we analyzed two cohorts of patients: The TNBC cohort included 72 female patients (mean age 55.97) and the METABRIC cohort included 293 female patients (mean age 63.35).
Data exclusions	Single cell data exclusion criteria were predetermined based on quality: Reads with multiple mapping positions were excluded; Cells with less than 1000 UMIs were discarded from the analysis. In the TNBC cohort, two patients were excluded from the analysis due to S100A4/PDPN values 3 SD above average. 4 patients were excluded from CD3 analysis due to unusually high background staining that could not be interpreted. All other scores collected were included in the analyses. In the METABRIC cohort 5 patients were excluded from the analysis due to S100A4/PDPN values 3 SD above average. For regional analysis of the METABRIC cohort, due to the small size of tumor cores, only samples in which 0.05 < ca/total ROI < 0.95 were included (n=219/288 patients).
Replication	All replication attempts were successful. Mouse experiments were performed on at least 3 biological replicates, in at least 2 independent experiments, as stated in the figure legends. For all IHC and MxIF staining experiments, preliminary staining was performed on n=3-5 samples, and then all slides of the same cohort were stained and imaged together unless indicated otherwise.
Randomization	All mice purchased together at the same age were randomized to the different groups of NMF, 2W, 4W and Mets
Blinding	Blinding was not done or needed for mouse experiments since all data was quantified and analyzed automatically. Staining, imaging, and processing of the raw human patient imaging data was performed in a blinded manner.

Reporting for specific materials, systems and methods

We require information from authors about some types of materials, experimental systems and methods used in many studies. Here, indicate whether each material, system or method listed is relevant to your study. If you are not sure if a list item applies to your research, read the appropriate section before selecting a response.

Materials & experimental systems

n/a	Involved in the study
☐	☒ Antibodies
☐	☒ Eukaryotic cell lines
☒	☐ Palaeontology
☐	☒ Animals and other organisms
☐	☒ Human research participants
☒	☐ Clinical data

Methods

n/a	Involved in the study
☒	☐ ChIP-seq
☐	☒ Flow cytometry
☒	☐ MRI-based neuroimaging

Antibodies

Antibodies used

Antibody Conjugation Clone Source Cat# Lot# Target species Application Dilution/Amount
EpCAM Alexa flour 488 G8.8 Biolegend 118210 b285223 mouse FACS analysis and sorting 1:100
EpCAM FITC G8.8 eBioscience 11579182 mouse FACS analysis and sorting 1:100
EpCAM PE/Cy7 G8.8 Biolegend 118215 b282356 mouse FACS analysis and sorting 1:100
CD45 BV711 30-F11 Biolegend 103147 b294297 mouse FACS analysis and sorting 1:100
CD45 APC 30-F11 Biolegend 103112 b247957 mouse FACS analysis and sorting 1:100
Ter119 Pacific blue Ter119 Biolegend 116232 b281640 mouse FACS analysis and sorting 1:100
PDPN APC 8.1.1 Biolegend 127410 b268805 mouse FACS analysis and sorting 1:100
PDPN APC/Cy7 8.1.1 Biolegend 127417 mouse FACS analysis and sorting 1:100
PDPN biotin 8.1.1 Biolegend 127404 b275382 mouse FACS analysis and sorting 1:200
Propidium iodide - - Sigma Aldrich P4170 mouse FACS analysis and sorting 1:1000
S100A4 - polyclonal Abcam ab41532 gr3246704-1 mouse, human Immunofluoresence 1:600
PDPN - polyclonal R&D Systems AF3244 wuf0318041 mouse Immunofluoresence 1:200
PDPN - D2-40 Biolegend 916605 b260223 human Immunofluoresence 1:200

Cytokeratin 7 - EPR17078 Abcam ab181598 gr324132-2 mouse Immunofluoresence 1:400
Pan-cytokeratin - AE1/AE3 Dako M3515 10151746 human Immunofluoresence 1:400
DAPI - - Biolegend 422801 B239813 - Immunofluoresence 1:1000
CD3 - D4V8L Cell Signaling 99940 human Immunofluoresence 1:400
CD45 - D9M8I Cell Signaling 13917 human Immunofluoresence 1:800
Ly-6C PerCP/Cy5.5 HK 1.4 Biolegend 128011 b282010 mouse FACS analysis and sorting 1:100
I-A/I-E APC/Cy7 M5/114.15.2 Biolegend 107628 b257359 mouse FACS analysis and sorting 1:100
HLA-DR - EPR3692 Abcam ab92511 human Immunofluoresence 1:600
a-SMA - 1A4 Sigma Aldrich A2547 huma/mouse Immunofluoresence 1:1000
a-SMA FITC 1A4 Sigma Aldrich F3777 huma/mouse FACS analysis 1:800
NT5E/CD73 - D7F9A Cell Signaling 13160 b55227 human Immunofluoresence 1:400
CD25 Brilliant Violet 711 PC61 Biolegend 102049 mouse FACS analysis 1:100
CD69 APC H1.2F3 Biolegend 104513 mouse FACS analysis 1:100
Ghost Dye Violet 450 - - TONBO 13-0863-T100 d0863100619133 - FACS analysis 1:500
Cytokeratin 8 - TROMA-1 Merck MABT329 mouse Immunofluoresence 1:200
Bovine anti-Goat HRP polyclonal Jackson 805-035-180 goat Immunofluoresence 1:400
Goat anti-Rabbit HRP polyclonal Jackson 111-035-144 132523 rabbit Immunofluoresence 1:400
Goat anti-Mouse HRP polyclonal Abcam 97040 gr3255988-5 mouse Immunofluoresence 1:400
Opal 520 Reagent Opal 520 - PE FP1487001KT 2474643 - Immunofluoresence 1:400
Opal 570 Reagent Opal 570 - PE FP1488A 2340753 - Immunofluoresence 1:400
Opal 620 Reagent Opal 620 - PE FP1495 2340757 - Immunofluoresence 1:400
Opal 650 Reagent Opal 650 - PE FP1496A 2399454 Immunofluoresence 1:400
Opal 690 Reagent Opal 690 PE FP1497A 2399456 - Immunofluoresence 1:400
1X Plus Amp Diluent - - PE FP1498 2511604 - Immunofluoresence 1X

Validation

All antibodies were tested by the manufacturer for the relevant applications to ensure specific staining to the antigen without cross-reactivity. In addition, we used for flow cytometry were calibrated on live mouse cells to ensure specific staining prior to use for FACS analyses and sorting. All antibodies used for immunofluorescence and immunohistochemistry of FFPE sections were calibrated on sections from the relevant target species, i.e. human or mouse, to ensure specific staining prior to staining of samples for analysis.

Eukaryotic cell lines

Policy information about cell lines

Cell line source(s)

4T1 mouse mammary carcinoma cells stably expressing firefly luciferase (pLVX-Luc) were kindly provided by Dr. Zvi Granot, Hebrew University of Jerusalem. E0771 mouse mammary carcinoma cells were kindly provided by Dr. Ronen Alon, The Weizmann institute if Science.

Authentication

4T1 line was purchased by Zvi Granot from the ATCC. We profiled the cells transcriptionally by bulk RNA-seq and also confirmed the expression of luciferase. E0771 cells were transcriptionally profiled as well.

Mycoplasma contamination

All cell cultures were tested negative for mycoplasma contamination.

Commonly misidentified lines
(See ICLAC register)

No commonly misidentified lines were used

Animals and other organisms

Policy information about studies involving animals; ARRIVE guidelines recommended for reporting animal research

Laboratory animals

Wild-type BALB/c and B57BL/6 female mice at the age of either 8 or 12 weeks.

Wild animals

The study did not involve wild animals.

Field-collected samples

The study did not involve samples collected from the field.

Ethics oversight

All animal studies were conducted in accordance with the regulations formulated by the Institutional Animal Care and Use Committee (IACUC; protocol # 40471217-2; 09720119-1; 00470120-2).

Note that full information on the approval of the study protocol must also be provided in the manuscript.

Human research participants

Policy information about studies involving human research participants

Population characteristics

Relevant covariates; age, BRCA status, invasion to lymph nodes, tumor size, recurrence-free period, overall survival period.

Recruitment

Whole tumor sections from 5 ER+ and 6 TN breast cancer patients were retrieved and obtained from the Israel National Biobank for Research (MIDGAM; https://www.midgam.org.il/) under MOH IRB# 130-2013 and IRB # 8736-11-SMC.
A tissue microarray (TMA) containing cores from 72 TNBC patients (3 cores per patient) with matching H&Es, and whole tissue sections from a subset of 12 patients from this cohort, was retrieved from the archives of Sheba Medical Center under IRB #

8736-11-SMC.
A TMA containing cores from 293 patients, with mixed breast cancer subtypes, was retrieved from from the METABRIC study.

Ethics oversight

Tumor sections from 5 ER+ and 6 TN breast cancer patients were obtained from MIDGAM under MOH IRB# 130-2013 and IRB # 8736-11-SMC, and a tissue microarray (TMA) containing cores from 72 TNBC patients (3 cores per patient), with matching H&Es, and whole tissue sections from a subset of 12 patients from this cohort, were retrieved from the archives of Sheba Medical Center under IRB # 8736-11-SMC. All clinical data were collected following appropriate ethical approvals. For the TNBC cohort: approval by the Sheba Medical Center Institutional Review Board (IRB; protocol # 8736-11-SMC) with full exemption for consent form for anonymized samples. For samples collected from the Israel National Biobank for Research: Ministry of Health (MOH) IRB approval (MIDGAM; protocol # 130-2013): These samples were collected from patients who provided informed consent for collection, storage, and distribution of samples and data for use in future research studies.
For the METABRIC study, appropriate ethical approval from the institutional review board was obtained for the use of biospecimens with linked pseudo-anonymized clinical data as detailed previously (Curtis et al, 2012).

Note that full information on the approval of the study protocol must also be provided in the manuscript.

Flow Cytometry

Plots

Confirm that:

☒ The axis labels state the marker and fluorochrome used (e.g. CD4-FITC).

☒ The axis scales are clearly visible. Include numbers along axes only for bottom left plot of group (a 'group' is an analysis of identical markers).

☒ All plots are contour plots with outliers or pseudocolor plots.

☒ A numerical value for number of cells or percentage (with statistics) is provided.

Methodology

Sample preparation

Mouse tumors or normal mammary fat fads were excised post-mortem, immediately after sacrificing the mice.

Instrument

FACS analyses were done using BD LSR II and FACS sorting was performed using BD FACSAria Fusion.

Software

FACS Diva v8 software was used for operating BD flow cytometry devices and collecting the data. Further analysis was performed using FlowJo software.

Cell population abundance

The abundance of the relevant cell populations is mentioned in supplementary figure 1a.

Gating strategy

The following steps describe the gating strategy as is depicted in supplementary figure 1a.
1. Negative staining for PI,
2. FFC/SSC exclusion of particles with FFC <≈ 30k.
3. Negative staining for Ter119.
4. Negative staining for CD45.
5. Negative staining for EpCAM.

☒ Tick this box to confirm that a figure exemplifying the gating strategy is provided in the Supplementary Information.